



## Article

# Hydrothermal Alteration Mapping Using Landsat 8 and ASTER Data and Geochemical Characteristics of Precambrian Rocks in the Egyptian Shield: A Case Study from Abu Ghalaga, Southeastern Desert, Egypt

Hatem M. El-Desoky<sup>1</sup>, Andongma W. Tende<sup>2</sup> , Ahmed M. Abdel-Rahman<sup>1</sup>, Antoaneta Ene<sup>3,\*</sup> ,  
Hamdy A. Awad<sup>4</sup>, Wael Fahmy<sup>1</sup>, Hamada El-Awny<sup>1</sup> and Hesham M. H. Zakaly<sup>5,6</sup>

<sup>1</sup> Geology Department, Faculty of Science, Al-Azhar University, Cairo P.O. Box 11884, Egypt; heldesoky@azhar.edu.eg (H.M.E.-D.); kady2040@azhar.edu.eg (A.M.A.-R.); wael\_fahmy50@azhar.edu.eg (W.F.); hamadaghanem.88@azhar.edu.eg (H.E.-A.)

<sup>2</sup> Department of Geology, Kano University of Science and Technology, Wudil 713101, Nigeria; andongmatende@gmail.com

<sup>3</sup> INPOLDE Research Center, Faculty of Sciences and Environment, Department of Chemistry, Physics and Environment, Dunarea de Jos University of Galati, 47 Domneasca Street, 800008 Galati, Romania

<sup>4</sup> Geology Department, Faculty of Science, Al-Azhar University, Assiut Branch, Assiut 71524, Egypt; hamdiawaad@gmail.com

<sup>5</sup> Institute of Physics and Technology, Ural Federal University, 620002 Yekaterinburg, Russia; h.m.zakaly@azhar.edu.eg

<sup>6</sup> Physics Department, Faculty of Science, Al-Azhar University, Assiut 71524, Egypt

\* Correspondence: antoaneta.ene@ugal.ro



**Citation:** El-Desoky, H.M.; Tende, A.W.; Abdel-Rahman, A.M.; Ene, A.; Awad, H.A.; Fahmy, W.; El-Awny, H.; Zakaly, H.M.H. Hydrothermal Alteration Mapping Using Landsat 8 and ASTER Data and Geochemical Characteristics of Precambrian Rocks in the Egyptian Shield: A Case Study from Abu Ghalaga, Southeastern Desert, Egypt. *Remote Sens.* **2022**, *14*, 3456. <https://doi.org/10.3390/rs14143456>

Academic Editor: Nicola Casagli

Received: 7 June 2022

Accepted: 7 July 2022

Published: 18 July 2022

**Publisher's Note:** MDPI stays neutral with regard to jurisdictional claims in published maps and institutional affiliations.



**Copyright:** © 2022 by the authors. Licensee MDPI, Basel, Switzerland. This article is an open access article distributed under the terms and conditions of the Creative Commons Attribution (CC BY) license (<https://creativecommons.org/licenses/by/4.0/>).

**Abstract:** This study evaluates the geological attributes of rocks within the Abu Ghalaga area using spatial, geochemical, and petrographic approaches. ASTER and Landsat imagery processed using band ratio and principal component analysis were used to map hydrothermal alterations, while a regional tectonic evaluation was based on automated extraction of lineaments from a digital elevation model. Geochemical and petrographic analyses were then employed for discrete scale evaluation of alteration patterns of rocks across the study location. Based on satellite image processing, alteration patterns across the study area are widespread, while evidence from lineament analysis suggests a dominant NW–SE tectonic trend accompanied by a less dominant ENE–WSW direction. The different rock units exposed in the studied district are arranged chronologically from oldest to youngest as arc metavolcanic group (basalt and rhyolite), arc metagabbro–diorite, gneissose granite (granodiorite and tonalite), and dykes (aplite and felsite). Various types of igneous and metamorphic rocks have propylitic, phyllic, and argillic zones. Geochemical data indicate that the studied rocks are classified into granite, granodiorite, gabbroic diorite, and gabbro. Geochemically, the rocks have a sub-alkaline magma type. The granodiorite–tonalite is derived from the calc–alkaline magma nature, while gabbro and diorite samples exhibit tholeiitic to calc–alkaline affinity. The tectonic setting of the studied rocks trends toward volcanic arc granite (VAG). Based on petrographic, geochemical, and remote analyses, sericitization, chloritization, epidotization, kaolinitization, carbonatization, and silicification are the main alteration types present in the study area. As a result of lineaments analysis, the existing fractures and structural planes form valid flow paths for mineral-bearing hydrothermal solutions.

**Keywords:** Landsat 8; ASTER; hydrothermal alteration; Wadi Abu Ghalaga; Southeastern Desert

## 1. Introduction

Remote sensing and geographic information systems constitute an integral part of geological investigations and have been sufficiently developed as coveted tools in the field of mineral exploration, where they have been successfully employed to map numerous

mineral resources, such as gold, copper, iron, and cassiterite. Remote sensing surveys in exploration programs are highly reliant on the identification of distinct spectral patterns that are related to hydrothermal alterations known to have a proximal relationship with specific mineral deposit types. For example, Ref. [1] identified the presence of alteration halos of hydroxyl-bearing minerals in close association with copper mineralization, while phyllic alteration has been identified near copper mineralization within the Central Iranian Cenozoic magmatic belt [2]. In the electromagnetic spectrum, spectral wavelengths in the range of 0.4–2.5  $\mu\text{m}$  extending from the visible, near-infrared, and short-wave infrared are considered inherent for geological studies with moderate- to low-temperature attributes, since the reflection of sunlight is permitted within this region [3]. According to [4], laboratory data suggest the spectral ranges from 0.4 to 1.1  $\mu\text{m}$  are invaluable in detecting iron oxide and hydroxides such as limonite and goethite, while from 1.0 to 2.5  $\mu\text{m}$ , hydrous minerals such as sericite, phyllosilicate, clays, mica, and some sulfates can be detected. In most exploration studies, Landsat and ASTER data are commonly used in the mapping of hydrothermal alteration.

Regional evaluation of geological structures and their relationship to mineral deposit types can serve as optimizers in most exploration surveys. Inclusive mapping of hydrothermal alteration in association with geological structures has proven reliable in the identification of numerous mineral resources [5]. Geological structures are known to have fundamental control on the migration of mineral-bearing hydrothermal fluids, and at regional scale, these structures can be effectively identified and delineated from different spatial data [6]. Both semi-automated and manual approaches have been widely used for lineament detection, and in most cases, the effectiveness of these methods is highly dependent on the spatial data type and the intrinsic experience of the analyst. In arid and semi-arid regions such as the Arabian–Nubian Shield (ANS), remote sensing is largely effective due to proportionate exposure of the underlying bedrock type.

Regionally, the Arabian–Nubian Shield (ANS), which forms the northern extension of the East African Orogen (EAO), is made up of a collection of island–arc tectonic terranes divided by suture zones, large shear zones, and cryptic major high strain zones. Between 1000 and 530 Ma, the ANS evolved during a 450-million-year period, and its expansion represents complex crustal evolution as part of the Rodinia–Gondwana supercontinent cycle.

Wadi Abu–Ghalaga represents part of the Late Proterozoic Arabian–Nubian Shield (ANS), which in turn constitutes part of the larger Pan African orogeny (Figure 1). It lies between latitudes 24°15' and 24°25'N and longitudes 35°02' and 35°06'E. This district is located to the north of Gabal Hamata (which represents the central part of the Hamata sheet) and south Wadi El-Gemal between Gabal Sarobi in the East and Gabal Tarfawi in the West, and it covers about 550 km<sup>2</sup> of the Precambrian rocks and the Phanerozoic sedimentary rocks that are exposed at the eastern part of the area. It is easily accessible by traveling on the Red Sea asphalt road about 85 km south of Marsa Alam City, then turning west across Wadi Abu Ghusun, which crosses the studied area from the north.

The study area, which runs from northwest to southeast, divides the map into two sections. Granite porphyry and pink pegmatitic granites cut through metavolcanics (mainly metandesites) in the eastern portion. Ilmenite deposits surround gabbroic rocks in the western part, which are bounded on the western and southeast sides by biotite gneissose granites.

The Precambrian rocks of the Southeastern Desert of Egypt, including the study area, have been studied by [7–14]. The purpose of this paper is to study the Wadi Abu Ghalaga area and differentiate the hydrothermal alteration zones from their host rocks, as there are target localities for mineral exploration in such areas. To achieve the goal of this study, we used ASTER data for lithological discrimination and alteration zone extraction. Further, chemical analysis was used to illustrate the magma type, chemical affinity, and the tectonic setting of the Precambrian Rocks in the study area. Moreover, field trips were undertaken to verify the remote sensing results.

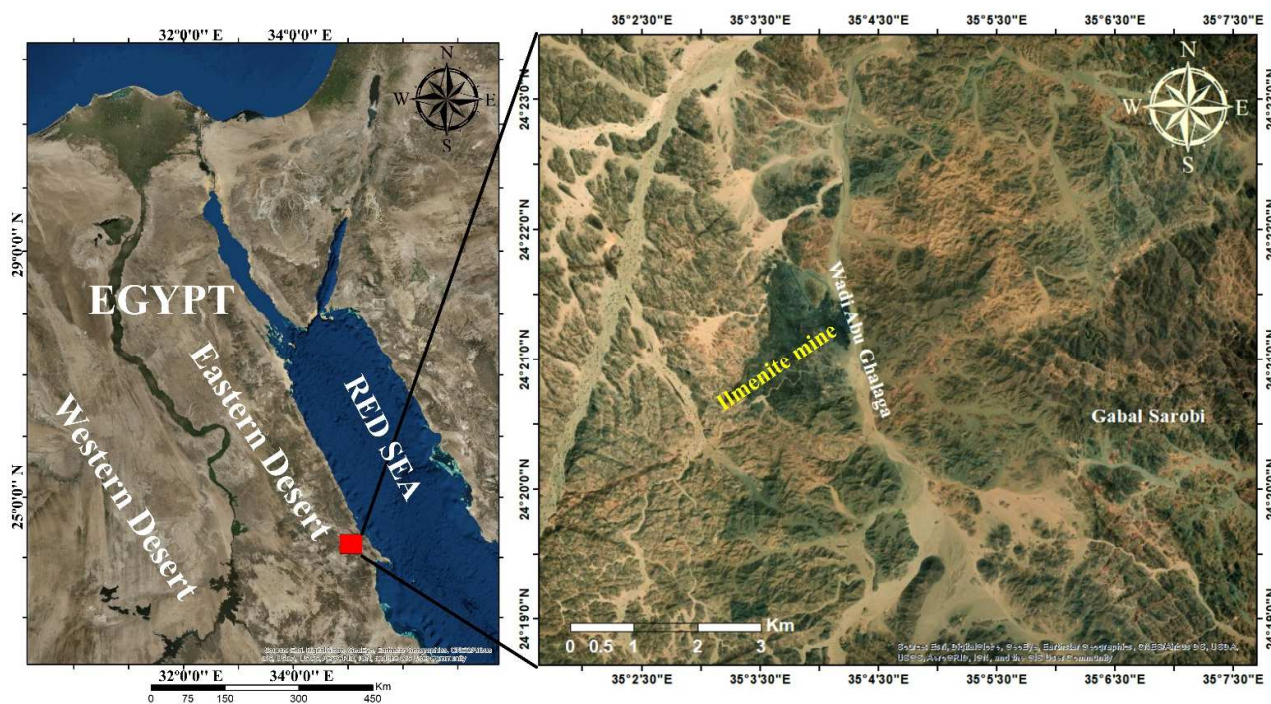


**Figure 1.** Location map of Wadi Abu Ghalaga.

## 2. Materials

### *Geologic Setting*

The Precambrian igneous–metamorphic complex (basement) of Egypt covers 100,000 km<sup>2</sup> and crops out along the Red Sea Hills in the eastern (Arabian) Desert, the southern Sinai Peninsula, and limited areas in the southwestern (Libyan) Desert (Oweinat area). The basement complex of Egypt is part of the Arabian–Nubian Shield (ANS). Generally, the ANS/basement of Egypt is comprised of three main tectonostratigraphic units (e.g., [15] from the bottom upward as follows: (1) high-grade gneisses and migmatites, (2) arc-type volcanic/volcano-sedimentary units along with dismembered ophiolites, and (3) the Ediacaran Hammamat and Dokhan supracrustal sequences. Granitoids intrude all three units.

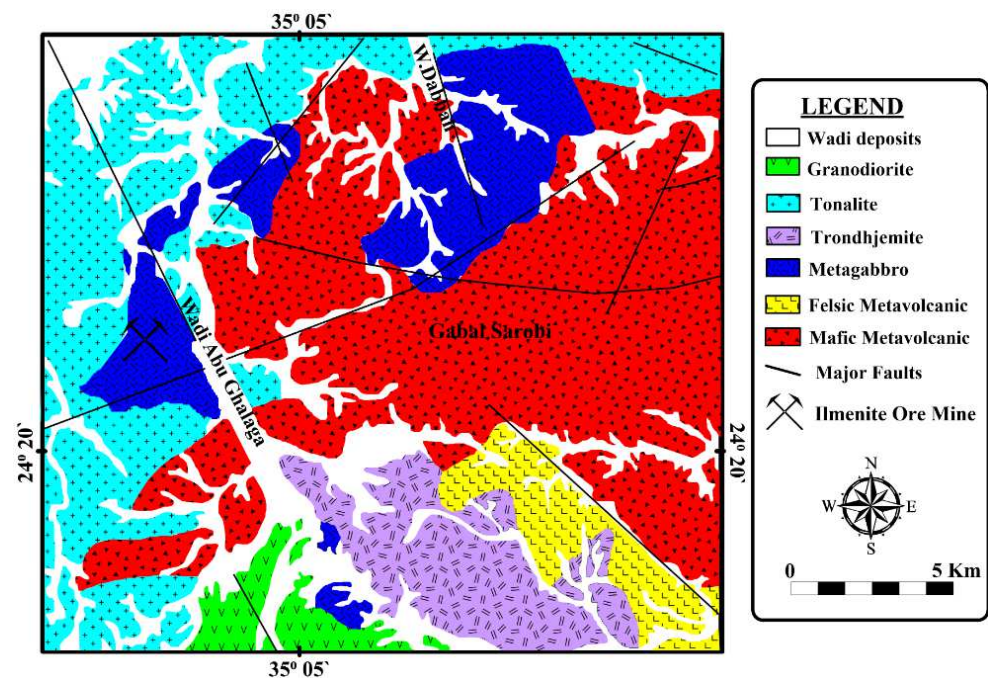
Ref. [16] divided the Egyptian basement complex into three stratified phases and granitic-rich intrusive rocks as follows: (1) the first (lower) sequence is represented by psammitic schists and gneisses, (2) the intermediate sequence is characterized by the prevalence of ophiolites, ophiolitic mélangé, and mafic to intermediate tholeiitic to calc-alkaline volcanic, and (3) the (youngest) sequence, which is dominated by felsic calc-alkaline to peralkaline volcanism and continental and molasse-type sedimentation. The present proposed classification is shown in Table 1.

The Precambrian rocks of the Wadi Abu Ghalaga area (Figure 2) are essentially Pan-African assemblage comprised of arc metavolcanic group (mafic, felsic, and rarely intermediate) and arc plutonic (gabbro–diorite and gneissose granites). The gneissose granite is represented by granodiorite and tonalite. These rock units are dissected by several dykes. Based on field relations, the rock units exposed in the area can be listed according to their chronological sequence as follows:

1. Dykes (youngest).
2. Gneissose granitite (granodiorite–tonalite).
3. Arc metagabbro–diorite.
4. Arc metavolcanics (basalt–rhyolite) (oldest).

**Table 1.** Major tectonic events and geochronology of the Neoproterozoic basement complex of Egypt [16–18].

	Rock Units	Age	Authors
Post-orogenic stage	Post-orogenic to anorogenic; Ultrabasic–basic intrusion, Felsites and A-type granites (El-Sibai–Gharib).	610–550	[16,19]
	Hammamat group (sandstone, conglomerate, greywacke, and volcanoclastics).	600–585	[20,21]
Orogenic stage	Dokhan volcanics (andesite and rhyolite flows, pyroclastics, and dyke swarms).	600–550	[19,22]
	Calc–alkaline granites (quartz diorite–trondhjemite–tonalite–granodiorite).	800–614	[16,19,23]
	Island arc assemblage: arc metavolcanics and metagabbro–diorite complexes.	850–620	[19,24,25]
	Ophiolites sequence; Serpentinites, metagabbro, old metavolcanics (OMV), sheeted dykes, and pillow lava.	810–730	[18,26]
Juvenile continental crust	Metasediments (gneisses, amphibolites and migmatites) (e.g., Hafafit, Sikait, Meatiq).	1770–1900	[4,27]

**Figure 2.** Detailed geologic map of Wadi Abu Ghalaga district [11].

The constructed regional geologic map for the studied district was modified after [11]. Based on the obtained present geological maps, field observations, structural relationships, and previous work, the exposed rock units in the study area are arc metavolcanics (mafic and felsic volcanic), Abu Ghalaga gabbro hosting Ti–Fe ores, syn-orogenic granites (granodiorite, tonalities, and diorites), and late- to post-orogenic granites. Field observation indicates they are moderate–hills, highly altered, fractured, massive, and sheared.

The arc metavolcanics are believed to be the oldest rock units cropping out in the Wadi Abu Ghalaga area. They occupy the eastern part of the study area as a NW–SE elongated belt. Field observations indicate that these rocks are massive submarine lava flows and pyroclastic mostly of mafic and felsic composition.

Locally, the lava shows pillow structure, especially at Wadi Sarobi and Wadi Qulan El-Atshan. Pillowed structure of some basalts and quench textures displayed by the volcanic rocks of Wadi Ranga indicate submarine extrusion of these rocks. The basic metavolcanics cover about 200 km<sup>2</sup> and crop out as two big belts of moderate to high elevations and

rugged hilly country. This is overlain by felsic metavolcanics from the east (and along the length of the Wadi Abu Ghalaga intruded by arc plutonic (gabbros and granites) in the center). The southern belt is traversed by Wadi Reidi and Wadi Qulan El-Atshan, where they were overlain by felsic metavolcanics from the east and intruded by the arc granitoids from the west. Structural contact between the mafic metavolcanics and felsic metavolcanics is commonly observed. The mafic metavolcanics are intercalated with the felsic metavolcanics, as seen at Wadi Qulan El-Atshan. They are essentially metabasalts with rare metaandesites (Figure 3A). The mafic to intermediate lava flows are characterized by deep blackish and dark greyish colors and are fine- to medium-grained. Field observation indicates they are moderate—hills, highly altered, fractured, massive, and sheared.

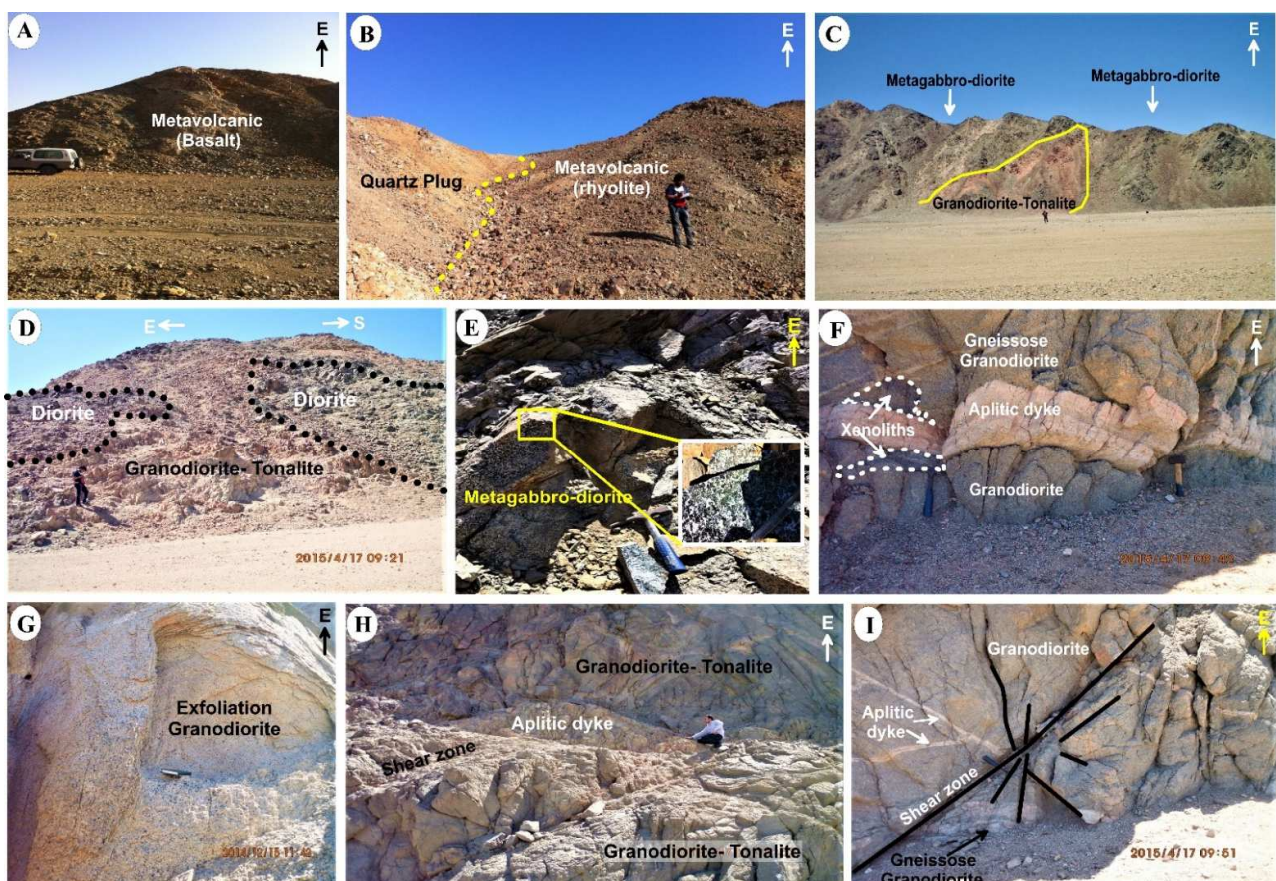


**Figure 3.** Field photographs of the of Abu-Ghalaga area show: (A) moderate—hills of metavolcanics blocks (metabasalts). (B) Contact between quartz plugs and metavolcanics (metarhyolites). (C) and (D) Granodiorite-tonalite intruding metagabbro-diorite. (E) Hand specimen consists of light- and dark-colored metagabbro-diorite. (F) Buff-colored felsic dyke and xenolith of mafic rocks (metagabbro-diorite) in gneissose granodiorite-tonalite. (G) Exfoliation of granodiorite-tonalite. (H) Off-shoot of aplitic dyke within the gneissose granodiorite-tonalite. (I) Gneissose granodiorite is affected by aplitic dykes along the shear zone.

Felsic metavolcanics are found in the southeastern part of the Wadi Abu Ghalaga area and form a large, elongated belt of moderate to high elevations and rugged, hilly country. They cover about 50 km<sup>2</sup> and crop out at Wadi Qulan El-Atshan, Wadi Dendikan, Wadi Ranga, and Wadi Reidi. They are overlain from the east by the Hammamat molasse-type sediments and intruded by arc gabbro-diorite and gneissose granites. They are locally extensively dissected by quartz plugs, and basic and acidic dykes, and exhibit well-developed vertical to sub-vertical joints (Figure 3B). The felsic flows are comprised of metarhyolites and rare metadacites. Metarhyolites in the Wadi Abu Ghalaga area are characterized by porphyries of quartz (white color) and orthoclase (buff color). These rocks

are massive, fine-grained, hard, and usually characterized by a buff or reddish color, as the K-feldspar crystals give their color to the rock (Figure 3B).

The arc plutonic rocks are comprised of gabbro–diorite and gneissose granite and cover a considerable part of the study area. They intrude the arc mafic metavolcanics and are injected by the arc granitoids of Abu Ghusun pluton, resulting in a hybrid zone of diorite along the contact.

Abu Ghalaga metagabbro–diorite rocks intrude the arc metavolcanics sequence and gneissose granites (granodiorites and tonalites) with clear thermal and tectonic contacts (Figure 3C,D). Metagabbro–diorite may enclose angular to subrounded fragments from the mafic metavolcanics, especially near their contacts. Diorites are light grey to greenish–grey color, coarse- to medium-grained, highly jointed, highly fractured, high relief, and occasionally foliated. These rocks are essentially composed of plagioclase, hornblende, biotite, pyroxene, and quartz with opaque constituents, and are intruded by granodiorite–tonalite (Figure 3D).

Metagabbro–diorite occurs as massive rocks of medium- to coarse-grain and with a dark grey color. They are commonly intensely jointed, fractured, and highly altered in many parts, especially along the fault planes. They exhibit dark greenish–grey color on a fresh surface, are massive, have dykes, and are fractured. They are composed mainly of plagioclase, clinopyroxenes, and hornblende with rare amounts of quartz (Figure 3E). Metagabbro–diorite (hosting Ti–Fe ores) is exposed to an elongated body striking NNE–SSE and dipping gently NNE (angle of dip about  $25^\circ$ ), covering about 6 km<sup>2</sup>. It represents the main mass of the Abu Ghalaga ilmenite mine. Several small outcrops are sporadically distributed along Wadi Abu Ghalaga and Wadi Um Selim (Figure 3E).

Two main rock types represent the gneissose granites (granodiorite and tonalite), which can be differentiated in the field according to their color, mineralogical composition, and visible texture. The northern pluton (Abu Ghusun) crops out along Wadi Abu Ghusun where the arc gneissose granite intrudes the arc metavolcanics and is intruded by Abu Ghalaga metagabbro–diorite (Figure 3C). Field evidence strongly suggests that the diorite and granodioritic rocks have been formed by contamination of granitic magma during reaction with the previously existing gabbroic rocks [7]. Generally, they are pinkish white to whitish–grey color and medium- to coarse-grained (Figure 3D). The mafic bodies enclosed in granodiorite are mainly refractory xenoliths or enclaves. The gneissose granites, especially to the NW of the mapped area, are seen to carry small bodies of gabbro as xenoliths (Figure 3F), with predominant xenoliths and alignment of mafic minerals in the form of gneissose texture (Figure 3F). The granodiorite–tonalites are commonly highly fractured, jointed, and characterized by high relief and exfoliation (Figure 3G). Gneissose granites (granodiorite–tonalite) are affected by apilitic dykes along the shear zone (Figure 3F,H,I).

Wadi Abu Ghalaga district is variably deformed, injected by numerous dykes (apilitic and felsic), veins, joints, and plugs of different shapes and compositions invading all the rock units cropping out in the study district. Most of the investigated dykes (apilitic and felsic) have an NE trend, and these dykes are usually light grey to buff in color and medium- to coarse-grained (Figure 3F,H,I). These dykes are widely distributed in the study district and invaded all different rock units. They are comprised of rhyolitic and granitic dykes penetrating gneissose granites (granodiorite–tonalite). The quartz plugs are generally medium- to coarse-grained white color. These plugs were formed from fluid flow controlled by small, deep-seated faults, which provided a low-resistance path for hydrothermal solutions (Figure 3B).

Structurally, the whole area has been subjected to considerable tectonic movements, especially those accompanying the intrusion of the biotite gneissose granites. These movements resulted in the appearance of joints and faults in the ilmenite body; the joints strike NW–SE, dipping  $20^\circ$ NE, while the faults have a NW direction [7]. Quartz veins and joints are most widely distributed among all the Abu Ghalaga rock units.

### 3. Methodology

#### 3.1. Landsat Imagery

Cloud-free Landsat 8 operational land imager (OLI) imagery with path number 173 and row number 043 captured on 24 January 2021 was downloaded from the United States Geological Survey Agency Earth Resource Observation and Science (USGS-EROS) website, <http://earthexplorer.usgs.gov>, accessed on 29 August 2021. The Landsat 8 OLI system, designed by Ball aerospace technology, operates from a conventional height of 705 km with an equatorial crossing time of 10.00 am  $\pm$  15 min. It circumnavigates the earth every 16 days (except for the highest polar latitude) and has a scene size of 170 km  $\times$  185 km. Generally, this system senses geoinformation within spectral wavelengths ranging from 0.483 to 2.330  $\mu$ m, covering the visible to infrared regions. Spatially the Landsat 8 OLI system can be divided into 11 bands, which include the visible (Bands 1, 2, and 3), red (Band 4), near infrared (Band 5), short-wave infrared (SWIR) (Bands 6 and 7), panchromatic (Band 8), cirrus (Band 9), and thermal (Bands 10 and 11) bands. Information capture from the Landsat 8 OLI system is generally within a spatial resolution of 30 m except for the panchromatic band, which obtains information at 15 m, and the thermal bands, which operate at a spatial resolution of 100 m. Table 2 illustrates the band characteristics of the Landsat OLI system.

**Table 2.** Technical characteristics of Landsat 8 OLI data.

	Bands	Wavelength (Micrometers)	Resolution (Meters)
Band 1	Coastal aerosol	0.43–0.45	30
Band 2	Blue	0.45–0.51	30
Band 3	Green	0.53–0.59	30
Band 4	Red	0.64–0.67	30
Band 5	Near Infrared (NIR)	0.85–0.88	30
Band 6	SWIR 1	1.57–1.65	30
Band 7	SWIR 2	2.11–2.29	30
Band 8	Panchromatic	0.50–0.68	15
Band 9	Cirrus	1.36–1.38	30
Band 10	Thermal Infrared (TIRS) 1	10.6–11.19	100
Band 11	Thermal Infrared (TIRS) 2	11.50–12.51	100

#### 3.2. Advanced Spaceborne Thermal Emission and Reflection Radiometer (ASTER) Imagery

ASTER Level 1T data, ID AST\_L1T\_00303312007082439\_20150518215126\_80884, obtained on 31 March 2007, was obtained from the United State Geological Survey Agency Earth Resource Observation and Science (USGS-EROS) website <http://earthexplorer.usgs.gov> (accessed on 29 August 2021). Basically, this is a multi-spectral imagery system launched onboard the NASA terra spacecraft in December 1999 in a collaboration between NASA (Washington, DC, USA) and the Japanese Ministry of Trade and Industry (MITI) (Tokyo, Japan). The ASTER system operates from a conventional height of 705 km and has an equatorial crossing of 10:30 am (north to south) defined by a repeated cycle of 16 days and offering a spatial resolution of 15 to 90 m across 14 bands. Specifically, the visible and near-infrared (VNIR) bands offer a spatial resolution of 15 m across three bands, while the short-wave infrared (SWIR) band offers a spatial resolution of 30 m across six bands. The thermal infrared (TIR) bands offer a spatial resolution of 90 m across five bands. Table 3 illustrates the basic specifications of the ASTER imagery.

**Table 3.** Technical characteristics of ASTER data.

Band	Label	Wavelength (μm)	Resolution (m)	Nadir or Backward	Description
B1	VNIR_Band1	0.520–0.60	15	Nadir	Visible green/yellow
B2	VNIR_Band2	0.630–0.690	15	Nadir	Visible red
B3N	VNIR_Band3N	0.760–0.860	15	Nadir	Near infrared
B3B	VNIR_Band3B	0.760–0.860	15	Backward	
B4	SWIR_Band4	1.600–1.700	30	Nadir	Short-wave infrared
B5	SWIR_Band5	2.145–2.185	30	Nadir	
B6	SWIR_Band6	2.185–2.225	30	Nadir	
B7	SWIR_Band7	2.235–2.285	30	Nadir	
B8	SWIR_Band8	2.295–2.365	30	Nadir	
B9	SWIR_Band9	2.360–2.430	30	Nadir	
B10	TIR_Band10	8.125–8.475	90	Nadir	Long-wave infrared
B11	TIR_Band11	8.475–8.825	90	Nadir	or thermal IR
B12	TIR_Band12	8.925–9.275	90	Nadir	
B13	TIR_Band13	10.250–10.950	90	Nadir	
B14	TIR_Band14	10.950–11.650	90	Nadir	

### 3.3. Digital Elevation Model

Digital elevation models (DEM) can be best regarded as a continuous spatial representation of ground surface topography or elevation [28]. Hence, their application in geology is highly valuable for elucidating the regional structural architecture of rocks and regions. In this study, the ASTER DEM, launched in 1999, was downloaded from the United States Geological Survey Agency Earth Resource Observation and Science (USGS-EROS) website, <http://earthexplorer.usgs.gov> (accessed on 29 August 2021) and used for lineament generation. The ASTER DEM, provided free-of-charge by NASA and Japan's MITI, consists of a  $1^\circ \times 1^\circ$  tile size and 30 m spatial resolution of elevation data spanning from  $83^\circ\text{N}$ – $83^\circ\text{S}$ . These data were developed by combining 1.3 million level 1A scene images obtained between 1 March 2000 and 30 November 2013. DEM development involved stacking all individual cloud masks and non-cloud mask scenes, followed by the application of a suitable algorithm to remove unwanted data. In this study, DEM was used for the extraction of lineament data within the study area. The preference for DEM was due to its high resolution and its ability to extract lineaments of geological origin [29].

### 3.4. Preprocessing

Preprocessing mainly involved conversion of digital numbers to reflectance. Both Landsat 8 OLI Collection 2 Level 2 imagery and ASTER L1T imagery were subjected to atmospheric correction using top of the atmosphere reflection algorithms. TOA involved the conversion of digital numbers for every band into a physically interpretable measure referred to as surface reflectance [30]. This process consisted of two steps: radiometric calibration involving the conversion of digital to radiance, followed by conversion of radiance to atmosphere reflectance.

$$L_\lambda = \text{gain} * \text{DN} + \text{bias}$$

where:

$L_\lambda$  represents the cell value as radiance

DN is the cell value for digital number

gain represents the gain value for the specific band

bias represents the bias value for the specific band

Equation (2) was used to convert radiance to reflectance

$$P_{\lambda} = \pi * L_{\lambda} * d^2 / ESUN_{\lambda} * \cos\theta_s$$

where:

$P_{\lambda}$  represents unitless planetary reflectance

$L_{\lambda}$  represents spectral radiance

$d$  is the Earth–Sun distance in astronomical units

$\theta_s$  represents the solar zenith angle

### 3.5. Image Processing

#### 3.5.1. Band Ratio

Band-ratio analyses have been widely applied to mineral exploration to detect hydrothermal alterations that may be related to mineral deposits [31–33]. According to [34], band-ratio processing of satellite data is often employed to emphasize specific anomalies in the target data. Generally, band-ratio analysis is critical in emphasizing specific features not visible on individual bands [35], and selection of the most suitable bands for ratio analysis depends on the spectral properties of the rock or minerals and their relative abundance [36]. Statistically, band ratio can be computed by dividing the digital number of a given band by the digital number of another band. Equation (1) illustrates the basic equation for band-ratio analysis [31,32].

$$Br = (B1)_i / (B2)_j \quad (1)$$

where B1 and B2 are the specific bands, and  $i$  and  $j$  represent the digital numbers within these bands. In this study, band ratios 6/7, 6/5, and 4/2 from Landsat 8 OLI imagery were used to enhance clay, ferric, and ferrous iron alterations, while band ratios 4/6, 5/6, 5/8, 2/1, and  $(5/3 + 1/2)$  from ASTER Level 1T imagery were used to enhance argillic, phyllic, propylitic, ferric, and ferrous iron alterations.

#### 3.5.2. Principal Component Analysis

Principal component analysis (PCA) is generally considered a more advanced tool for statistical data reduction, and in satellite image processing analysis, PCA is highly critical for unraveling alteration evidence that may depict mineralization patterns [2,31,37,38]. Basically, PCA transforms several correlated spectral bands into a smaller number of uncorrelated spectral bands called principal components [39]. In exploration studies, PCA has been applied to both ASTER and Landsat imagery [40,41]. In this study, PCA was applied to Landsat bands 2, 4, 5, 6, and bands 2, 5, 6, and 7 as a means of enhancing information related to iron and clay alterations, respectively. Similarly, PCA was applied to ASTER bands 1, 4, 6, and 7; ASTER bands 1, 3, 5, and 6; and ASTER bands 1, 3, 5, and 8 as a means of enhancing information on argillic, phyllic, and propylitic alterations, respectively.

#### 3.5.3. Lineament Extraction

Geological structures are pivotal constraints for mineral deposit formations, and on a regional scale, these features can be mapped from a variety of spatial data [42]. In previous studies, extraction of geological lineaments has been implemented using manual, automated, or semi-automated methods [43,44]. However, in this study, lineaments were extracted automatically. According to [45], automated methods have been credited for their reproducibility and efficiency. The spatial extraction of lineaments from DEM was facilitated by specific software settings (Table 4) on PCI Geomatica v10.0. Lineament extraction was followed by spatial and statistical analyses, including orientation analysis using rose plots [46] and lineament length and lineament density analyses [47].

**Table 4.** Software specification for lineament extraction.

Sn	Parameter Settings	Parameter Value
1	Filter Radius (Pixels)	5
2	Edge Gradient Threshold	10
3	Curved Length Threshold (Pixels)	10
4	Line fitting Error Threshold (Pixels)	3
5	Angular difference Threshold (Degrees)	30
6	Linking Distance Threshold (Pixels)	20

### 3.6. Fieldwork and Laboratory Techniques

Field study included a description of field relations and structural settings of the rock units exposed in the studied area. More than 50 rock samples representing different rock types were collected. In addition, petrographic studies of 50 selected samples were done in detail using an Olympus polarized microscope at Al-Azhar University, Egypt. At the Egyptian Mineral Resources Authority's Central Laboratories, major and uncommon rare-earth elements were analyzed in about 28 samples using a Philips X-ray fluorescence (XRF) spectrometer PW/2404 equipped with a Rh radiation tube with eight analyzing crystals (EMRA).

## 4. Results

Pervasive, selectively pervasive (in which certain minerals or minerals in textural sites are replaced), or non-pervasive alteration are all possible (for instance, only adjacent to fractures). In most hydrothermal systems, alteration affects a volume of rock many times that of the ore body. As a result, a hydrothermal system's alteration presents a far bigger target for identification and mapping than a deposit, and it is widely utilized in exploration as a marker of proximity to ore. Temperature, pressure, fluid composition (concentrations of  $H^+$ ,  $Cl^-$ ,  $CO_2$ , F, B,  $Na^+$ ,  $K^+$ ,  $H_2S$ , and other elements in solution), host-rock composition before alteration, and the mass balance of rock and fluid (fluid/rock ratio) all influence mineral assemblages in hydrothermally altered rock [48]. There are three main sources of thermal fluids resulting in hydrothermal alteration: (1) near-surface and groundwater (generally meteoric or seawater), (2) magma volatiles exsolved from melt (termed juvenile water), and (3) fluids originating from dehydration upon metamorphic reactions.

Phyllic alteration (sericite and muscovite) occurs in metarhyolite, gabbro–diorite, granodiorite, and tonalite. Sericite is one of the most common types of hydrothermal alteration found in felsic igneous rocks. Sericitization is a process in which plagioclases and other minerals are altered to sericite through the action of low-temperature hydrothermal solutions on rocks. The replacement of plagioclase by sericite is associated with the alteration of muscovite to chlorite. The altered plagioclase crystals accompany the alteration of fluids in two ways: (1) selective replacement of plagioclase by sericite; and (2) replacement of  $Ca^{2+}$  by  $Na^{1+}$  in the surviving plagioclase to form slightly more sodic plagioclase [49].

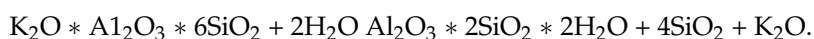
Phyllic alteration originates late in the hydrothermal system's evolution and frequently overprints potassic and chlorite–sericite alteration zones, particularly in their upper and peripheral regions. Quartz, sericite, and pyrite are the three most important minerals. In hand samples, phyllic-altered rock appears bleached and practically textureless, as these minerals grow over the older rock texture. K-feldspar, kaolinite, biotite, calcite, rutile, topaz, anhydrite, and tourmaline are some of the other gangue minerals that can be found. Phyllic alteration takes place at moderate temperatures (200–450 °C) and is caused by a moderately to strongly acidic fluid, resulting in the addition of  $H^+$  and dissolving of K, Na, Ca, Mg, Ti, and Fe from the rocks, as seen in the replacement of K-feldspar with sericite:



Propylitic alteration (epidote and chlorite) is concentrated in metarhyolite, metaandesite, gabbro–diorite, and tonalite rocks. Epidotization is a transformation process during

which secondary epidote originates at the expense of plagioclase crystals. This type of transformation is often connected with chloritization. Propylitic alteration is widespread around most porphyry deposits, extending up to several kilometers out from the ore body with progressively decreasing strength of development. Greenschist-facies metamorphism alteration assemblages are like propylitic alteration assemblages. Epidote, chlorite, and calcite are essential minerals. Pyrite is commonly found. Iron oxides, sericite, and apatite are some of the other minerals. Propylitic alteration occurs when H<sub>2</sub>O, CO<sub>2</sub>, and, in many cases S<sub>2</sub>, are added to host rocks without considerable acid–base metasomatism, metal addition, or leaching at temperatures between 250 and 400 degrees Celsius.

Argillic alteration is encountered in all rocks and occurs at relatively shallow levels of the hydrothermal system above and peripheral to the phyllic zone and may occur locally. Clay minerals are essential minerals (montmorillonite, kaolinite). Kaolinitization is a transformation of aluminosilicates to kaolin in acidic rocks (rhyolite and/or granite) or intermediate rocks (andesite). Kaolinitization is also locally concentrated; due to this, potash feldspar crystals represent massive kaolin pseudomorphs; the reaction can be shown as follows:



Biotite, chlorite, illite, pyrophyllite, sulphides, quartz, and andalusite are some of the other minerals found. Clay minerals are generated as a result of acid leaching of feldspars and mafic silicates during strong, low-temperature metasomatism (100–300 °C), which results in argillic alteration. The formation of hydrothermal minerals in the studied area depends on several factors, including (1) temperature, (2) pressure, (3) rock type, (4) permeability, (5) hydrothermal fluid composition, and (6) duration of alteration or extent of reaction.

Rock type affects hydrothermal alteration mainly through changes in permeability. In fact, the initial primary mineralogy has limited effects on hydrothermal alteration, particularly at temperatures >200 °C. For example, quartz, albite, K-feldspar, chlorite, epidote, calcite, and pyrite are the dominant alteration minerals associated with rhyolite, andesite, and basalt [50]. Permeability is a major factor affecting hydrothermal alteration. Hydrothermal alteration involves the interaction of fluids with minerals. The availability of fluids and contact between minerals and fluids is therefore of central importance. At low permeability and associated with limited availability and flow of hydrothermal fluids, primary minerals and rocks can withstand alteration at high temperatures. Hydrothermal alteration associated with fluids with low magma gas input is dominated by zeolites, chlorite, epidote, prehnite, quartz, sulfides, and carbonates.

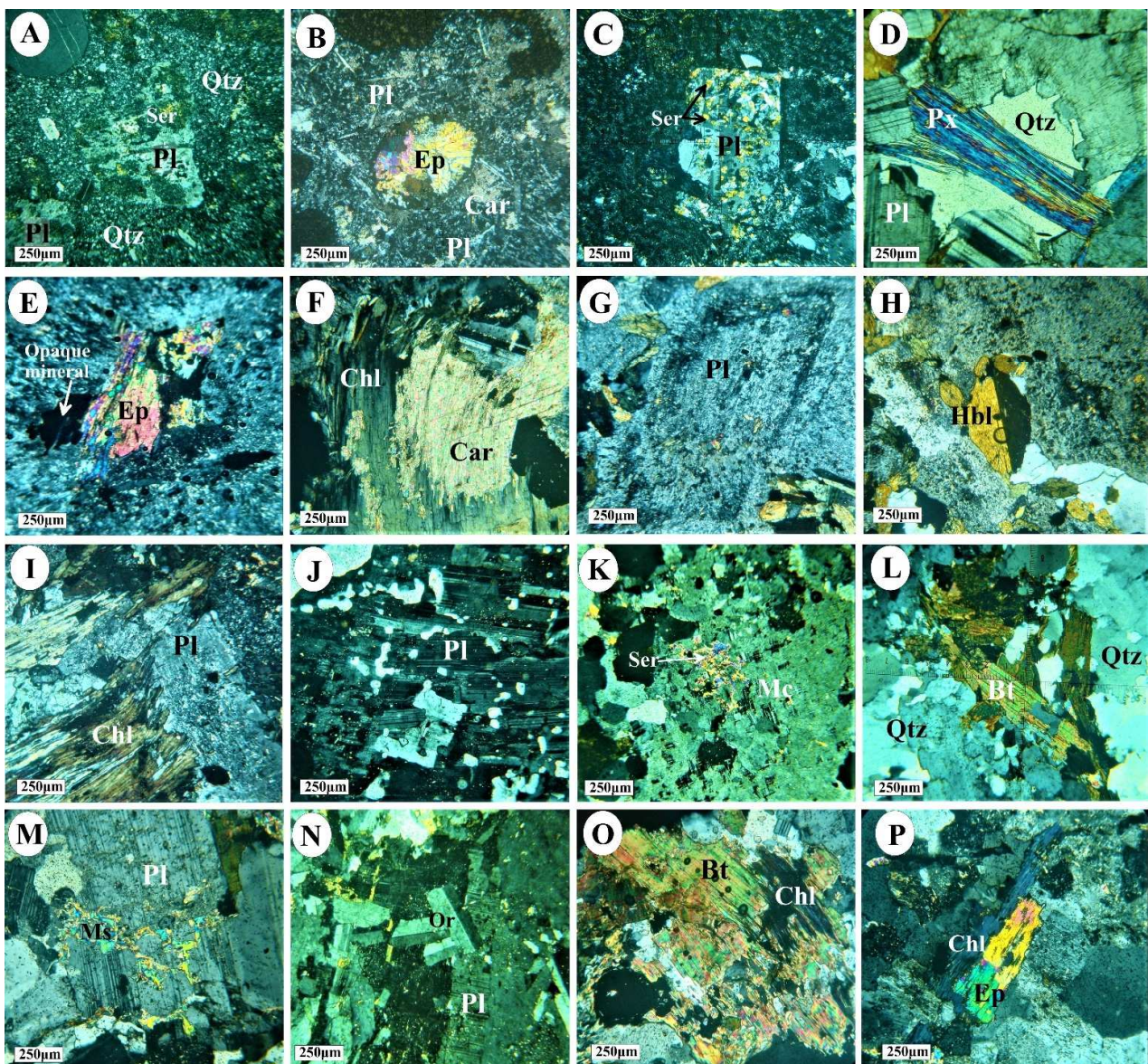
#### 4.1. Petrographic Characterization

A petrographic description of the mineralogical composition and textural features characterizing the different rock units exposed in Abu Ghalaga district follows. These rock units are arranged chronologically from oldest to youngest as metavolcanics, metagabbros, diorite, and gneissose granites (biotite granodiorites and tonalites). The petrographic descriptions of rock types in the studied region are summarized in Table 5.

The metavolcanic rocks are represented by metarhyolite, metabasalt, and metaandesite. Metarhyolite is composed of phenocryst of quartz, sanadine, plagioclase altered to kaolinite, epidote, and sericite. These rocks are affected by carbonate–kaolinite–sericite alteration. They are characterized by spherulitic and porphyritic texture (Figure 4A). While metabasalt rocks are composed of fine grains of plagioclase and altered pyroxene, pyroxene minerals are altered by chlorite alteration. These rocks are distinguished by vesicular or spilite texture (Figure 4B). On the other hand, metaandesites range from fine to medium grains. They generally have porphyritic texture (Figure 4C), with phenocrysts of plagioclase, quartz, and pyroxene set in a groundmass of plagioclase, hornblende, chlorite, epidote, quartz, and iron oxides.

**Table 5.** Summary of the petrographic descriptions of different rock types in the study area.

Rock Types	Mineralogical Composition	Texture	Alteration Types
Metarhyolite	Quartz, sanadine, plagioclase	Spherulitic, porphyritic	Kaolinite, epidote, carbonate, sericite
Metabasalt	Plagioclase and pyroxene	Vesicular or spilitic	Chlorite
Metaandesite	Plagioclase, hornblende, pyroxene	Porphyritic	Chlorite, epidote.
Metagabbros	Clinopyroxene, plagioclase, and hornblende	Diabasic, subophitic, schiller	Epidote, chlorite, carbonate.
Diorite	Plagioclase, biotite, hornblende, and pyroxene	Hypidiomorphic	Epidote, chlorite, kaolinite.
Biotite granodiorites	Quartz, plagioclase, microcline, and biotite	Hypidiomorphic, poikilitic, graphic	Sericite, epidote.
Tonalites	Quartz, plagioclase, orthoclase, and biotite	Hypidiomorphic granular, gneissose	Chlorite, epidote, muscovite.

**Figure 4.** Photomicrographs showing some petrographic characteristics of Abu-Ghalaga under cross-polarized light (XPL): metarhyolite (A), metabasalt (B), metaandesite (C), metagabbro (C–F), quartz

diorite (G–I), biotite granodiorite (J–L), and tonalite rocks (M–P). (A) Porphyritic texture showing phenocryst of plagioclase (Pl) crystals within fine grains of quartz (Qtz). (B) Epidote (Ep) secondary mineral filling the vesicular texture. (C) Plagioclase altered (Pl) to saussuritization. (D) Schiller structure-associated subophitic texture. (E) Pyroxene (Px) altered to epidote (Ep). (F) Two stages of alteration: chloritization is formed as an alteration product of clinopyroxene, and carbonization mostly appears as large, stained, grained aggregates replacing chlorite (Chl). (G) Grains of sericitized plagioclase with fresh rims. (H) Baveno twinning of hornblende (Hbl). (I) Chlorite (Chl) after hornblende (Hbl) surrounding plagioclase (Pl). (J) Poikilitic and graphic textures. (K) Microcline (Mc) grain showing sericitized core. (L) Large biotite crystals (Bt). (M) Muscovite (Ms) after plagioclase (Pl). (N) Orthoclase (Or) crystals associated with plagioclase (Pl). (O) Violet irregular chlorite particles (Chl) after biotite (Bt). (P) Berlin blue interference color of chlorite (Chl) and well-developed epidote crystals (Ep).

The metagabbros are composed essentially of deformed clinopyroxene, plagioclase, and hornblende. Epidote, chlorite, and carbonate are the main secondary minerals, whereas quartz is less common. Opaque minerals occur in a high ratio in this rock as titaniferous-gabbros comprised of fresh, altered, and quartz-injected varieties. Plagioclase (An40–An60) is mostly calcic plagioclase (andesine to labradorite) forms as xenomorphic and subidiomorphic crystals up to 3.2 mm in length and 1.5 mm in width and showing percline and Carlsbad twinning. Occasionally, plagioclase crystals exhibit diabasic texture. Usually, they are clouded and altered to sericite and kaolinite. Pyroxene (augite) is found either as subidiomorphic or xenomorphic crystals (Figure 4D). It is characterized by high interference color and is usually altered to hornblende and chlorite (Figure 4F). In some parts, subophitic texture is associated with schiller structure (Figure 4D). Further, some pyroxene crystals are shown schiller structure. Quartz is rarely encountered as an essential mineral but sometimes exists in fair amounts, pointing to silica-metasomatism. It occurs as xenomorphic crystals fill the interstices between other minerals and shows slight undulose extinction (Figure 4D). Hornblende occurs as yellowish-brown subidiomorphic to xenomorphic crystals up to 3.4 mm in length and 1.7 mm in width. Sometimes it is enclosed within plagioclase crystals, forming a Baveno texture. Moreover, it is highly altered to chlorite and epidote along cracks and contains relics of pyroxene (Figure 4E). Epidote, chlorite, and carbonate are present as alteration products derived from the plagioclase minerals (Figure 4E,F). Opaque minerals are dark-colored particles dispersed between the other constituents and are commonly associated with chlorite and epidote (Figure 4E).

Diorites consist essentially of plagioclase, biotite, hornblende, and pyroxene, and quartz, epidote, chlorite, and opaque minerals are the main accessories. They are characterized by hypidiomorphic texture showing medium to coarse grains. The plagioclase is usually andesine (An42–An48) and reaches 1 mm in length. It is either fresh or much altered to kaolin and sericite at a low-temperature assemblage. Occasionally, plagioclase crystals are altered to sericite in the core of the crystals (Figure 4G). Alteration products of the plagioclase also includes saussuritization and kaolinitization (Figure 4G). The secondary quartz is dispersed in the interstitial spaces between the other mineral constituents (Figure 4H). The hornblende forms big, prismatic and foliated crystals and shows Baveno twinning (Figure 4H). Some hornblende phenocrysts occur as medium-grained subhedral crystals are slightly altered to chlorite (Figure 4I).

Biotite granodiorites are medium- to coarse-grained and greyish-white in color. They consist essentially of quartz, plagioclase, microcline, and biotite, with secondary minerals such as sericite, epidote, and opaques. The common textures in this type are hypidiomorphic, poikilitic, and graphic textures. Plagioclase is the main mineral constituent of the granodiorite. It also exhibits a cloudy surface due to alteration to epidote and sericite (Figure 4J). Potash-feldspar is represented by microcline altered to sericite (Figure 4K). Sometimes, quartz crystals show intergrowth with orthoclase, exhibiting graphic and gneissose textures (Figure 4J). Biotite occurs as subhedral, brown, elongated flakes, 0.4 mm long and 0.2 mm wide. It shows strongly dichroic, with masking of interference color and can be partially altered to chlorite (Figure 4L).

Tonalite, microscopically, is hypidiomorphic granular and usually shows some gneissose texture due to the subalignment of biotite and chlorite. It consists essentially of quartz, plagioclase, orthoclase, and biotite; chlorite, epidote, muscovite, and ore minerals represent the main accessories. The quartz forms big allotriomorphic crystals of about 0.6 mm diameter, which usually show strong undulose extinction. The plagioclase is mostly oligoclase (average composition Ab75An25), forming tabular crystals of about 0.4 mm diameter that contain spots of secondary muscovite in their central parts (Figure 4M). The crystals show good albite and albite–Carlsbad twinning but little or no zoning (Figure 4M). The potash–feldspar is mainly orthoclase and frequently subordinate to plagioclase (Figure 4N). It forms subhedral prismatic crystals of about 0.3 mm diameter, which are often relatively fresh. Biotite is the most predominant mafic mineral and is a dark yellowish–brown variety (Figure 4O). It occurs in small flakes (0.2 mm), which may aggregate with a few chlorite and epidote flakes (Figure 4P).

Briefly, the propylitic alteration (epidote and chlorite) is concentrated in metarhyolite, metaandesite, metabasalt, gabbro–diorite, and tonalite rocks, while phyllic alteration (sericite and muscovite) occurs in metarhyolite, gabbro–diorite, granodiorite, and tonalite. On the other hand, argillic alteration is encountered in all rocks.

#### 4.2. Geochemical Characterization

Twenty-eight rock samples representative of the studied rocks were chemically analyzed for major and trace elements, including nine samples of tonalite, four samples of granodiorite, four samples of diorite, and eleven samples of gabbro. The analytical results for major oxides and rare earth elements (REEs) in addition to calculated normative minerals are listed in Tables 6 and 7. Analysis of the studied tonalite and granodiorite rocks reveal an average SiO<sub>2</sub> content varying from 66.03 to 77.76 wt.% and high content of Al<sub>2</sub>O<sub>3</sub> (11.22–16.94 wt.%). Furthermore, TiO<sub>2</sub> content ranges from 0.1 to 0.86 wt.%, whereas Fe<sub>2</sub>O<sub>3</sub> content ranges from 1.03 to 5.24 wt.%. FeO ranges from 0.93 to 4.70 wt.%, CaO ranges from 0.77 to 4.45 wt.%, MgO ranges from 0.01 to 1.98 wt.%, Na<sub>2</sub>O ranges from 3.46 to 5.81 wt.%, K<sub>2</sub>O ranges from 0.4% to 1.93 wt.%, and they have low contents of MnO and P<sub>2</sub>O<sub>5</sub>, ranging from 0.01 to 0.07 wt.%.

Rare-earth element analyses show that the tonalite and granodiorite samples tend to be richer in Ce (7.32–20 ppm), Nd (7.4–45.01 ppm), and Y (1.5–54.7 ppm). On the other hand, tonalite, and granite show low enrichment in Dy, Er, Eu, and Sm. Meanwhile, SiO<sub>2</sub> contents in diorite and gabbro rocks range from 48.1 to 57.15 wt.%, Al<sub>2</sub>O<sub>3</sub> ranges from 13.5 to 20.54 wt.%, Fe<sub>2</sub>O<sub>3</sub> ranges from 5.97 to 12.56 wt.%, TiO<sub>2</sub> ranges from 0.5 to 4.89 wt.%, and P<sub>2</sub>O<sub>5</sub> ranges from 0.01 wt.% to 0.27 wt.%. The analyzed samples show a calc–alkaline composition, with MgO ranging from 3.61 to 10.23 wt.%, CaO ranging from 5.6 to 14.45 wt.%, Na<sub>2</sub>O ranging from 1.39 to 5.01 wt.%, and K<sub>2</sub>O ranging from 0.1 to 1.05 wt.%.

The normative compositions of the tonalite and granodiorite rocks show high values of quartz orthoclase, anorthite, albite, hypersthene, and diopside. They also show low contents of apatite, ilmenite, and magnetite. Meanwhile, the normative compositions in the diorite and gabbro rocks are quartz, orthoclase, anorthite, albite, hypersthene, ilmenite, oligoclase, and diopside. They also show low contents of apatite and hematite (Ha), as summarized in Tables 6 and 7.

The petrographic classification of the studied rock units was chemically confirmed by plotting the analytical data on an Or–Ab–An diagram. Geochemical classification of the studied rocks using an Or–Ab–An diagram shows that these rocks are plotted in the fields of granodiorite, tonalite, gabbro, and diorite. Based on the Ab–Or–An ternary diagram [51], the gabbro and diorite samples were plotted in the gabbro fields, while the granodiorite and tonalite plots were located near tonalite and granodiorite (Figure 5A).

**Table 6.** Major oxides (wt.%), trace elements (ppm), some elemental ratios, and CIPW norm of the studied tonalite, granodiorite, and diorite rocks.

Rock Type	Tonalite										Granodiorite					Diorite				
S. No.	1A	5A	8A	8A1	11A	17A	18A	47A	48A	Av	2A	4A	12A	19A	Av	3A	9A	10A	14A	Av
SiO <sub>2</sub>	75.65	70.36	75	77.76	66.03	73.26	77.37	73.48	75.36	73.81	75.54	69.7	76.36	70.41	73.00	57.15	54.82	54.34	54.71	55.26
TiO <sub>2</sub>	0.17	0.32	0.29	0.14	0.35	0.1	0.03	0.34	0.36	0.23	0.2	0.86	0.1	0.35	0.38	0.69	0.94	0.86	0.63	0.78
Al <sub>2</sub> O <sub>3</sub>	13.08	14.63	12.44	11.22	16.94	14.73	12.94	12.13	11.75	13.32	13.74	13.55	13.11	14.51	13.73	18.47	16.79	18.1	14.32	16.92
Fe <sub>2</sub> O <sub>3</sub>	1.8	3.5	3.85	1.99	3.62	1.72	1.03	3.4	2.93	2.65	2	5.24	1.27	3.14	2.91	6.3	8.77	8.18	8.91	8.04
FeO	1.62	3.14	3.5	1.8	3.3	1.55	0.93	3.1	2.64	2.40	1.8	4.7	1.14	2.83	2.62	5.7	7.9	7.4	8.02	7.26
MnO	0	0	0.01	0	0	0	0	0.01	0.01	0.00	0.01	0.01	0.01	0	0.01	0.01	0.02	0.02	0.02	0.02
MgO	0.58	1.63	0.71	0.61	1.98	0.32	0.01	1.14	0.75	0.86	0.31	1.65	0.03	1.23	0.81	3.61	5.72	5.27	7.65	5.56
CaO	1.56	2.65	2.84	1.85	4.28	2.6	1.71	4.54	2.72	2.75	0.77	2.54	1.24	3.56	2.03	5.68	7.77	9.02	9.86	8.08
Na <sub>2</sub> O	5.31	4.65	3.89	5.31	4.61	5.38	5.81	3.46	4.31	4.75	4.83	4.06	5.29	4.46	4.66	5.01	3.06	2.88	2.56	3.38
K <sub>2</sub> O	0.75	0.97	0.45	0.4	0.92	0.7	0.46	0.51	0.66	0.65	1.37	1.09	1.93	1.21	1.40	1.05	0.37	0.3	0.25	0.49
P <sub>2</sub> O <sub>5</sub>	0.02	0.06	0.01	0.01	0.03	0.01	0.01	0.03	0.02	0.02	0	0.07	0.01	0.05	0.03	0.11	0.06	0.09	0.01	0.07
Cl	0.01	0.01	0.01	0.01	0.01	0.01	0.01	0.01	0.01	0.01	0.01	0.01	0.01	0.01	0.01	0.01	0.01	0.01	0.01	0.01
SO <sub>3</sub>	0.04	0.02	0.02	0.02	0.02	0.02	0.01	0.01	0.01	0.02	0.01	0.04	0.01	0.01	0.02	0.04	0.03	0.01	0.02	0.03
LOI	0.74	0.88	0.19	0.41	0.9	0.89	0.49	0.65	0.81	0.66	0.93	0.88	0.39	0.78	0.75	1.57	1.33	0.63	0.76	1.07
Total	101.3	102.8	103.2	101.5	102.9	101.2	100.8	102.8	102.3	102.1	101.5	104.4	100.9	102.5	102.3	105.4	107.5	107.1	107.7	106.7
Na <sub>2</sub> O/K <sub>2</sub> O	7.08	4.8	8.64	13.3	5.01	7.7	12.63	6.78	6.53	8.1	3.53	3.72	2.74	3.7	3.4	4.8	8.3	9.6	10.24	8.2
Rare earth elements (ppm)																				
Ce	8.12	9.83	9.54	14.47	10.66	8.07	7.32	18.8	14.95	11.1	10.13	16	10.08	20	14.1	8.86	6	4.44	1.53	4.97
Dy	0	0	0	0	0	0	0	2.8	0.56	0.37	0	0	0	0	0.0	0	0	0	0	0.00
Er	0	0	0.08	0	0	0	0	4.22	3.57	0.87	0	0	0	0	0.0	1.13	2.2	0.66	0.22	0.86
Gd	0.85	1.66	4.26	2.34	1.72	0	0.04	8.45	5.74	2.78	0.18	3.21	0.41	1.37	1.3	6.8	8.5	5.48	6.23	6.11
Nd	15.7	21.11	26.19	17.04	27.86	7.4	5.18	35.6	34.5	21.8	13.4	45.02	15.8	23.5	24.4	57.68	74.18	50.99	40.28	51.8
Pr	0.68	2.7	3.82	1.83	3.15	3.74	2.19	6.6	4.4	3.23	0.22	3.33	1	5.7	2.6	7.3	9.99	8.34	9.69	8.58
Sm	0	0	0	0	0	0	0	2.7	0.75	0.38	0	0	0	0	0.0	0.17	0.11	0	0	0.06
Y	5.06	3.71	18.8	17.43	3.26	0	4.83	54.7	38.8	16.3	2.8	6.78	4.95	1.5	4.0	11.5	13.52	9.63	9.84	9.14
Yb	0.71	0.62	2.41	2.3	0.57	0	0.08	4.96	4.1	1.46	0.6	1	0.74	0	0.6	1.72	2.57	1.82	2.01	1.76
CIPW normative minerals																				
Q	38.0	30.87	43.03	40.77	22.71	32.89	38.23	38.2	38.67	35.93	40.42	33.03	35.27	30	34.7	-	9.69	9.08	-	4.7
Or	4.65	5.37	2.79	2.36	5.44	4.14	2.83	3.22	4.14	3.88	8.55	6.44	11.41	7.15	8.4	6.81	2.19	1.77	1.68	3.1
An	13.9	23.6	28.8	10.8	33.9	36.98	13.14	34.4	22	24.17	8.1	25.1	11.4	28.8	18.4	35.8	53.4	58.4	52.35	50.0
Ab	39.1	28.09	18.42	39.6	25.87	21.1	44.23	11.96	22.28	27.86	57.59	20.99	39.17	24.84	35.6	34.8	3.35	1.38	-	9.9
Di	-	-	-	2.78	-	-	0.36	4.18	1.68	2.25	-	-	-	1	1.0	1.74	2.65	6.77	15.72	6.7
Hy	2.04	6.41	3.38	1.58	7.42	2.06	0.64	7.31	6.55	4.15	1.57	7.01	0.97	4.6	3.5	17.57	17.27	15.31	27.2	19.3

Table 6. Cont.

Rock Type	Tonalite										Granodiorite					Diorite					
	S. No.	1A	5A	8A	8A1	11A	17A	18A	47A	48A	Av	2A	4A	12A	19A	Av	3A	9A	10A	14A	Av
Mt	1.35	5.07	2.89	2.89	5.25	2.49	1.49	0.26	0.22	2.43	1.51	7.6	1.84	4.55	3.9	0.49	12.72	11.86	0.72	6.4	
Ilm	0.18	0.61	0.31	0.27	0.66	0.19	0.06	0.37	0.39	0.34	0.22	1.63	0.19	0.66	0.7	0.78	1.79	1.63	0.74	1.2	
Ap	0.04	0.14	0.02	0.02	0.07	0.02	0.02	0.06	0.04	0.05	-	0.16	0.02	0.12	0.1	0.25	0.14	0.21	0.02	0.2	
c	0.56	1.34	0.31	-	0.7	0.47	-	-	-	0.68	2.01	1.28	0.13	-	1.1	-	-	-	-	0.0	
Hm	0.02	0.02	0.02	0.02	0.02	0.02	0.02	0.02	0.02	0.02	0.02	0.02	0.02	0.02	0.02	0.02	0.02	0.02	0.02	0.03	0.0
NS	0.07	0.07	0.02	0.04	0.04	0.0	0.0	0.0	0.0	0.03	0.02	0.07	0.02	0.0	0.0	0.04	0.04	0.05	0.04	0.0	

**Table 7.** Major oxides (wt.%), trace elements (ppm), some elemental ratios, and CIPW norm of the gabbroic rocks.

Rock Type	Gabbro											
S. No.	7A	15A	32A	33A	34A	35A	36A	37A	42A	45A	46A	Av.
SiO <sub>2</sub>	50.35	51.7	53.92	52.77	50.03	53.97	49.69	52.9	56.54	48.8	48.1	51.7
TiO <sub>2</sub>	0.87	1.08	0.64	1.11	4.35	0.94	4.89	1.48	0.5	0.58	0.51	1.5
Al <sub>2</sub> O <sub>3</sub>	17.45	15.21	20.54	18.6	14.5	18.94	13.5	18.14	14.33	16.36	19.01	17.0
Fe <sub>2</sub> O <sub>3</sub>	8.03	10.22	5.97	8.78	12.56	8.06	13.71	8.95	8.75	9.19	8.41	9.3
FeO	7.22	9.2	5.37	7.9	11.3	7.3	12.33	8.1	7.87	8.27	7.57	8.4
MnO	0.01	0.04	0	0.01	0.01	0.02	0.02	0.02	0.04	0.02	0.02	0.0
MgO	10.23	7.3	4.53	5.76	5.5	4.89	6.05	5.14	6.07	7.45	7.5	6.4
CaO	8.01	9.48	7.74	7.47	8.91	7.57	7.67	7.48	7.87	14.45	12.69	9.0
Na <sub>2</sub> O	2.38	2.92	4.22	3.61	2.84	3.91	2.9	3.44	3.22	1.55	1.39	2.9
K <sub>2</sub> O	0.1	0.4	0.45	0.21	0.21	0.19	0.24	0.36	0.65	0.35	0.34	0.3
P <sub>2</sub> O <sub>5</sub>	0.03	0.1	0.02	0.09	0.22	0.05	0.27	0.1	0.01	0.01	0.01	0.1
Cl	0.01	0.01	0.01	0.01	0.01	0.01	0.01	0.01	0.01	0.01	0.01	0.0
SO <sub>3</sub>	0.02	0.02	0.01	0.01	0.01	0.01	0.01	0.06	0.02	0.02	0.01	0.0
LOI	2.2	1.22	1.66	1.27	0.55	1.16	0.65	1.62	1.7	0.92	1.7	1.3
Total	106.91	108.9	105.08	107.6	111	107.02	111.94	107.8	107.58	107.98	107.2	108.1
Na <sub>2</sub> O/K <sub>2</sub> O	23.8	7.3	9.38	17.2	13.52	20.6	12.1	9.56	4.95	4.43	4.1	11.5
Rare earth elements (ppm)												
Ce	4.03	9.73	3.47	4.74	18.14	5.6	19.37	18.9	1.98	4.28	0.96	8.3
Er	0.08	3.11	0.5	2.83	12.88	2.1	16.6	3.85	0.56	0.61	0.48	4.0
Gd	3.56	10.44	3.54	7.23	14.29	6.2	14.6	7.6	6.72	7.37	8.5	8.2
Nd	35.94	77.25	39.2	80.1	263	63.2	333	1.04	32.8	35.5	28.3	89.9
Pr	7.6	10.9	8.12	9.13	12.3	8.3	11.4	9.7	10.2	15.65	11.8	10.5
Sm	0	1.66	0	0	2.79	0	3.02	0.28	0	0	2.79	1.0
Tb	0	0	0	0	2.72	0	3.6	0.07	0	0	0	0.6
Y	1.23	26.08	0	1.95	10.5	2.9	15.2	4.3	6.5	8.35	4.7	7.4
Yb	0.7	3.44	0	0.46	1.99	0.42	2.04	0.62	1.06	1.14	0.66	1.1
CIPW normative minerals												
Q	-	-	-	-	-	-	-	-	1.55	1.39	-	1.5
Or	0.68	2.69	2.94	1.39	1.42	1.25	1.63	2.39	4.36	4.36	2.3	3.7
An	61.47	51.3	48.8	51.4	51.1	49.1	47.4	52.3	44.8	44.4	47.1	45.4
Ab	-	4.72	26.37	16.98	3.31	21.29	4.56	13.72	8.99	9.56	12.96	10.5
Di	1.99	13.68	1.66	1.72	11.9	2.49	9.49	2.26	11.44	11.55	13.08	12.0
Hy	20.95	10.04	12.97	17.45	15.72	18.58	17.77	21.68	27.42	27.38	7.7	20.8
Mt	0.66	0.83	0.47	0.7	1.03	0.64	1.12	0.72	0.7	0.7	0.69	0.7
Ilm	1.02	1.26	0.72	1.27	5.08	1.07	5.74	1.7	0.58	0.58	0.6	0.6
Ap	0.06	0.21	0.04	0.19	0.47	0.1	0.57	0.21	0.02	0.02	0.02	0.0
Hm	0.03	0.03	0.02	0.02	0.03	0.02	0.03	0.02	0.03	0.03	0.03	0.0
NS	0.04	0.02	0.0	0.0	0.0	0.0	0.0	0.1	0.1	0.0	0.0	0.1
Ol	13.1	15.23	5.97	8.86	9.94	5.43	11.67	4.88	-	-	15.17	8.2

According to the Na<sub>2</sub>O + K<sub>2</sub>O versus SiO<sub>2</sub> diagram [52], the studied samples fall in the granite, granodiorite, gabbroic diorite, and gabbro fields (Figure 5B). The authors of [52] used a (Na<sub>2</sub>O + K<sub>2</sub>O)-SiO<sub>2</sub> binary diagram to differentiate between alkaline and sub-alkaline rocks (Figure 5C). According to this diagram, the investigated samples fall in the field of subalkaline (Figure 5C). On the other hand, they have meta-aluminous and peraluminous affinity according to the Al<sub>2</sub>O<sub>3</sub>/Na<sub>2</sub>O + K<sub>2</sub>O versus Al<sub>2</sub>O<sub>3</sub>/Na<sub>2</sub>O + K<sub>2</sub>O + CaO binary diagram [53], (Figure 5D). Based on the (Fe<sub>2</sub>O<sub>3</sub> + TiO<sub>2</sub>)-Al<sub>2</sub>O<sub>3</sub>-MgO ternary diagram of [54], the studied granodiorite and tonalite samples exhibit calc-alkaline nature, while gabbro and diorite samples exhibit tholeiitic to calc-alkaline affinity (Figure 5E). On the Al<sub>2</sub>O<sub>3</sub>-CaO-Na<sub>2</sub>O + K<sub>2</sub>O ternary diagram [55], the granodiorite and tonalite lie in the hyperaluminous field, while the gabbro and diorite samples fall in hyperaluminous to meta-aluminous field (Figure 5F). On the log Rb-(Y + Nb) and log Y-Nb discrimination

diagrams [56] to differentiate between the different tectonic settings of granitic rocks (Figure 6), the studied samples plot in the volcanic arc granites (VAG).

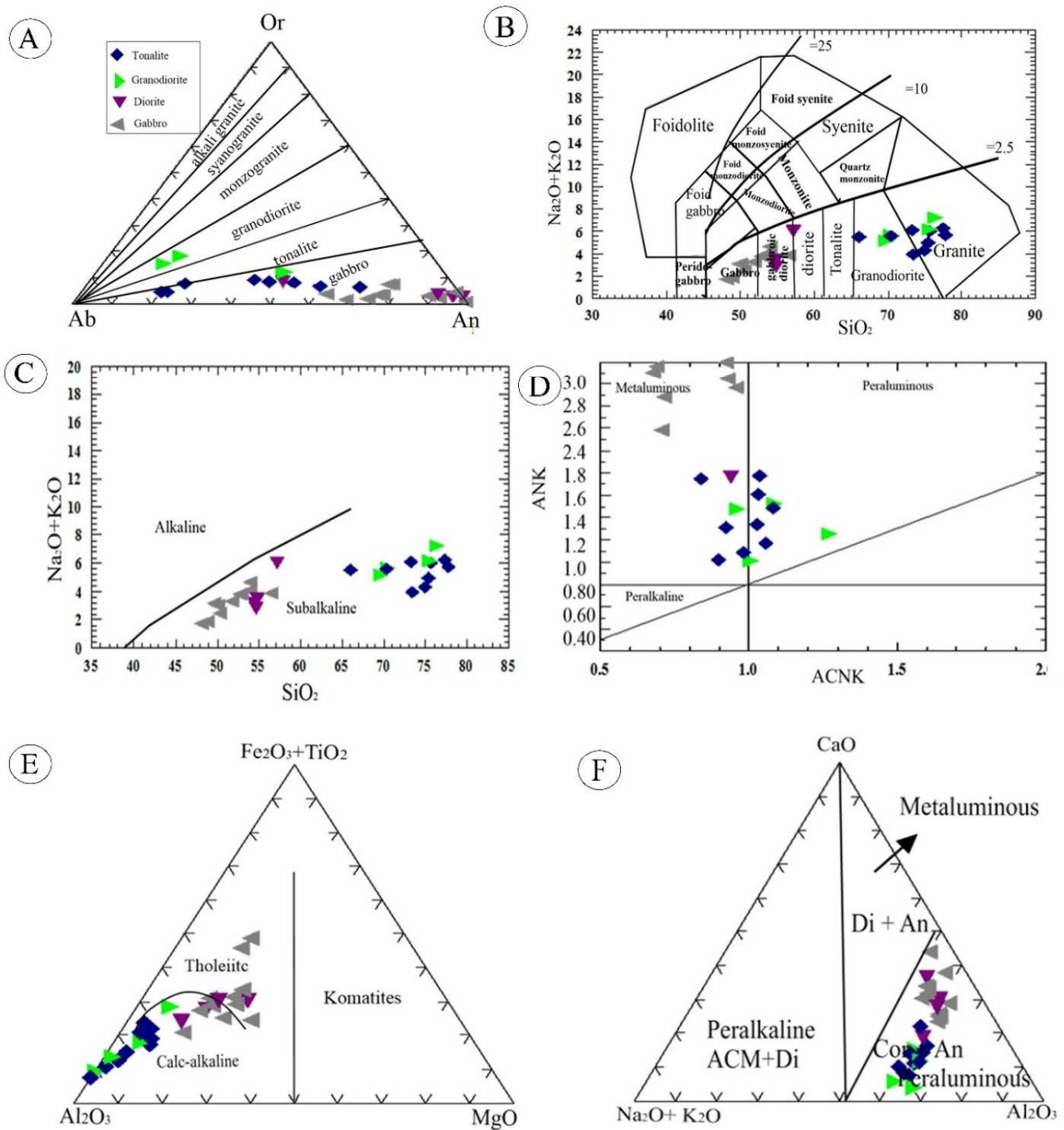


**Figure 5.** (A) Geochemical classification of the studied rocks of [51] based on the Ab–Or–An ternary diagram. (B) Chemical nomenclature of plutonic rocks using TAS diagram [57]. (C) Total alkali–silica variation diagram (Irvine and Baragar, 1971). (D) CNK variation diagram of the studied samples [53]. (E)  $(Fe_2O_3 + TiO_2)$ – $Al_2O_3$ – $MgO$  diagram for the studied rocks [54]. (F)  $CaO$ – $Na_2O + K_2O$ – $Al_2O_3$  diagram [58]. Symbols as in (Figure 5A).

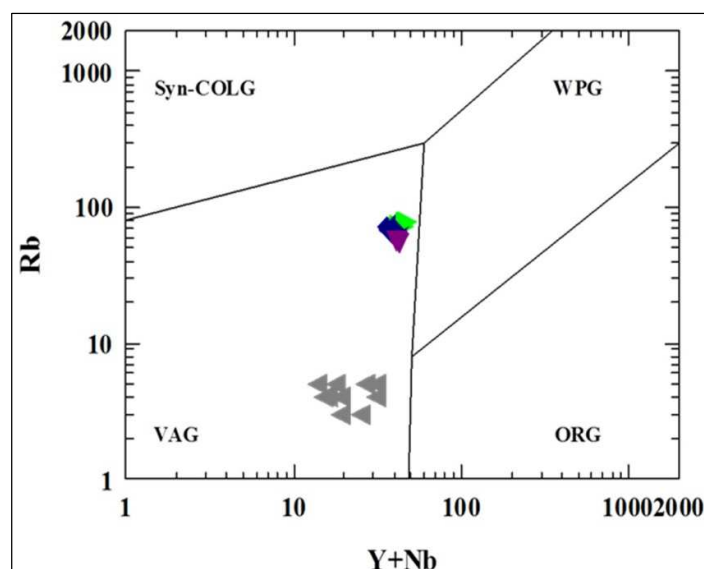


**Figure 6.** Rb–(Y + Yb) binary diagram [56]: VAG, volcanic arc granites; Syn-COLG, syn-collision granites; WPG, within plate granites; ORG, ocean ridge granites.

#### 4.3. Geochemistry of Hydrothermal Alteration

The Na<sub>2</sub>O–K<sub>2</sub>O binary diagram [59] indicates that most samples are impacted by sodic alteration, which is one of the most common kinds of alteration (Figure 7A). One of the most potent tools for evaluating hydrothermal alteration is the combination of petrography and bivariate plots. The magmatic samples had a low K/Al and alteration index ( $AI = 100 (MgO + K_2O) / (MgO + K_2O + CaO + Na_2O)$ ; Figure 7B) plotted against the chlorite–carbonate–pyrite index diagram (CCPI; Figure 7C). Except for gabbroic rocks, the geochemical indicators of the materials analyzed all point to albite alteration. On the other hand, the gabbroic samples plot as chlorite–carbonates, which is congruent with the petrographic results.

The type of altered minerals and the intensity of each rock unit alteration according to its lithogeochemistry is directly depicted by the “alteration box plot” by [60] which incorporates the Ishikawa alteration index (AI) [61] with the chlorite–carbonate–pyrite index (CCPI), (Figure 7D). Gabbroic rocks can be found at the top of the least-changed andesite–basalt box, whereas dioritic rocks can be found in the center (dacite). On the other hand, granitic rocks indicate a felsic propensity (tonalite and granodiorite) (rhyolite). K-silicate facies can be classified as (1) propylitic (containing epidote–chlorite alteration), (2) sericitic (containing K-feldspars that was converted to sericite, and (3) potassic (characterized by the alteration of K-feldspar into muscovite) subtypes. The present samples are plotted on the diagram (Figure 7E) of [62]. All samples fall in sericitic facies (due to sericitization processes) and gabbro–diorite samples close to the propylitic type. On the original alteration box plot, the distribution of the samples suggests that the dominant processes are carbonization and chloritization (Figure 7E).

#### 4.4. Alteration Mapping with Landsat 8 Imagery

Typically, Landsat rather than ASTER imagery of multispectral attributes is employed for mineral alteration mapping [63]; although considered primitive to ASTER data, Landsat’s synoptic view and wide coverage make it the preferred option for regional sensing and exploration. We illustrate spatial mapping of alterations using the band-ratio. A well-computed band ratio of 6/7 displayed spatial variations in clay alterations from blue (low) to red (high) pixels. Equally, band-ratio computations of 6/5 discriminated zones of ferrous iron alterations from blue to red pixels, while band ratio 4/2 essentially displayed variations in ferric iron intensity from blue to red pixels (Figure 8). A false-color composite

of 6/7, 6/5, and 4/2 suggested the presence of clay alteration as red pixels, ferrous iron alteration as green pixels, and ferric iron alteration as blue pixels (Figure 8).

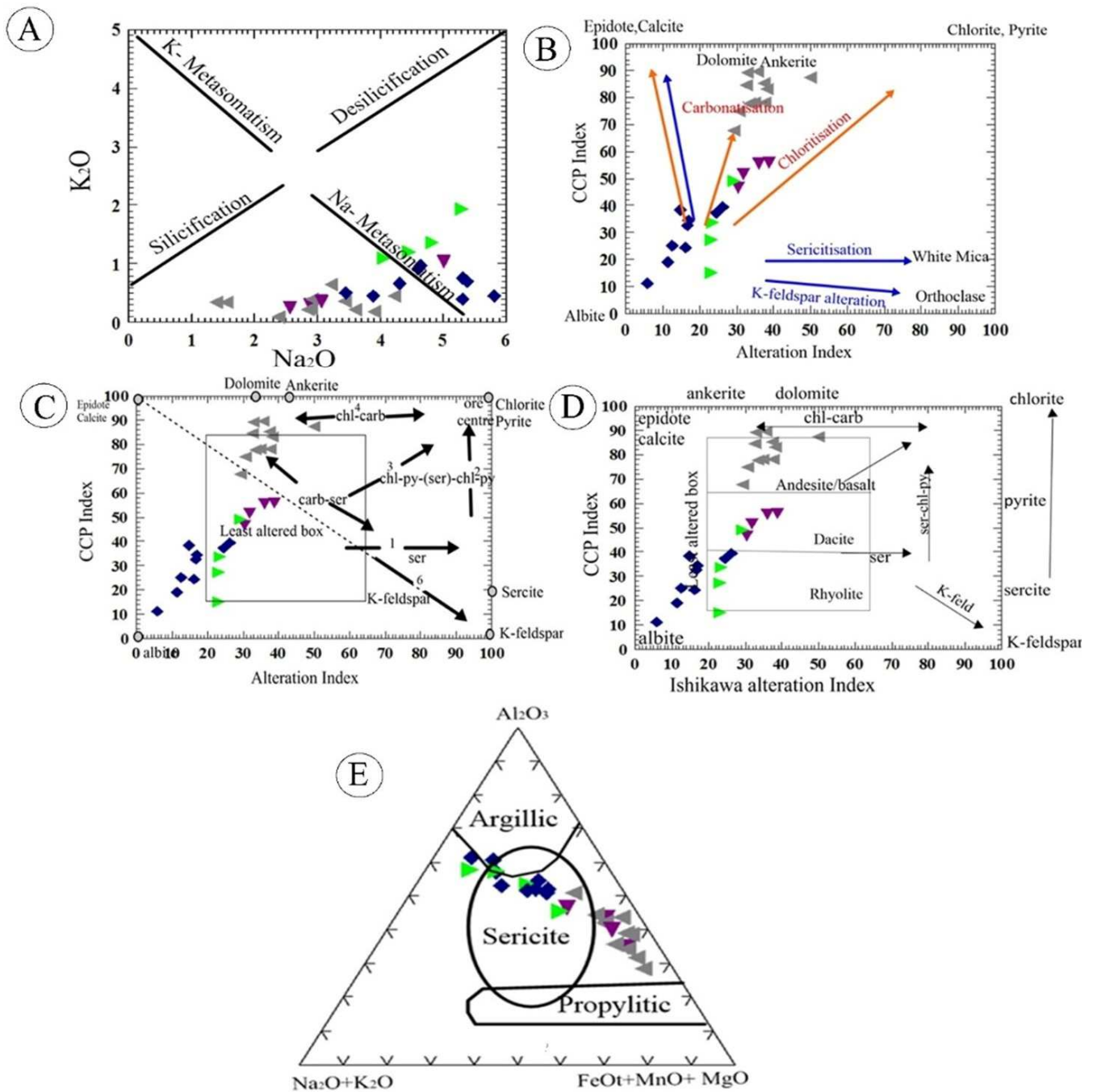


**Figure 7.** Different alteration diagrams; (A) Na–K binary diagram of [59]. (B) Chlorite–Carbonate–Pyrite Index [60] versus Alteration Index [61] of intrusive rocks of Abu Ghalaga on the “alteration box plot”. (C) CCPI versus AI for least-altered and altered samples [60]. (D) CCP Index [60] versus Ishikawa Alteration Index (AI) (Ishikawa et al., 1976);  $AI = 100(K_2O + MgO)/(K_2O + MgO + Na_2O + CaO)$ ;  $CCPI = 100(MgO + FeOT)/(MgO + FeOT + Na_2O + K_2O)$ . (E)  $Al_2O_3 - (Na_2O + K_2O) - (FeOT + MnO + MgO)$  ternary diagram of [62].

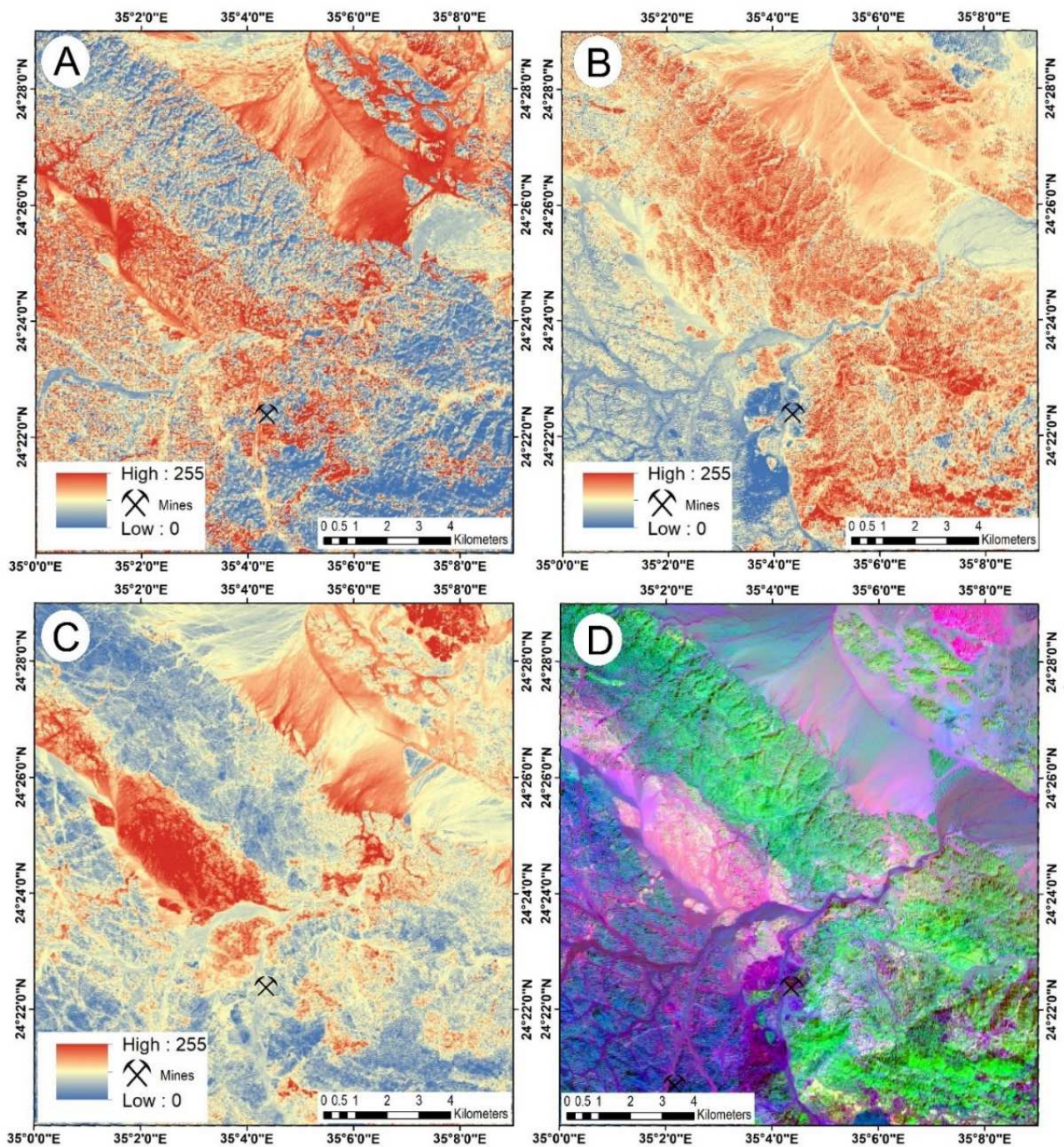


**Figure 8.** Band-ratio processing of Landsat 8 imagery: (A) Band ratio 6/7 for clay alteration mapping. (B) Band ratio 6/5 for ferric alteration mapping. (C) Band ratio 4/2 for ferrous iron alteration mapping. (D) False-color composite of 6/7, 6/5, and 4/2.

Based on spectral data, clay-bearing alterations are known to have significant reflectance on band 6 and very high absorption on band 7. Similarly, high reflectance for the ferrous iron alteration is observed on band 6, while a conspicuous absorption is also observed for band 5. For ferric iron alterations, high reflectance is observed for band 4 and high absorption for band 2 [64]. A false-color composite of 6/7, 6/5, and 4/2 suggests the presence of clay alteration as red pixels, ferrous iron alteration as green pixels, and ferric iron alteration as blue pixels (Figure 8). Within this image, zones of high clay alteration are observed as red pixels, while zones of ferric and ferrous iron alterations are

observed as green and blue pixels, respectively. In comparison to Landsat ETM imagery, band ratios 6/7, 6/5, and 4/7 are the spatial equivalence of the Chica–Olma ratio (5/7, 5/4, 3/1) as proposed by [65]. Based on previous studies, for example [37], the Landsat 8 band ratio corresponding to the Chica–Olma ratio has been highly reliable in mapping mineralization. Within the Egyptian desert, the Chica–Olma ratio has been used to map gold mineralization [66].

Spatial analysis of alteration variations by application of PCA is presented in Figure 9A. Based on Eigenvector loading, the application of PCA to bands 2, 4, 5, and 6 suggests information on iron alteration was successfully mapped into principal component band 4 as dark pixels. This is evident by high negative loading from band 4 accompanied by significantly high positive Eigenvector loading from band 2 (Table 8). The resultant PC band 4 was negated to display spatial variations related to the iron alteration from blue (low) to red (high) pixels (Figure 9).

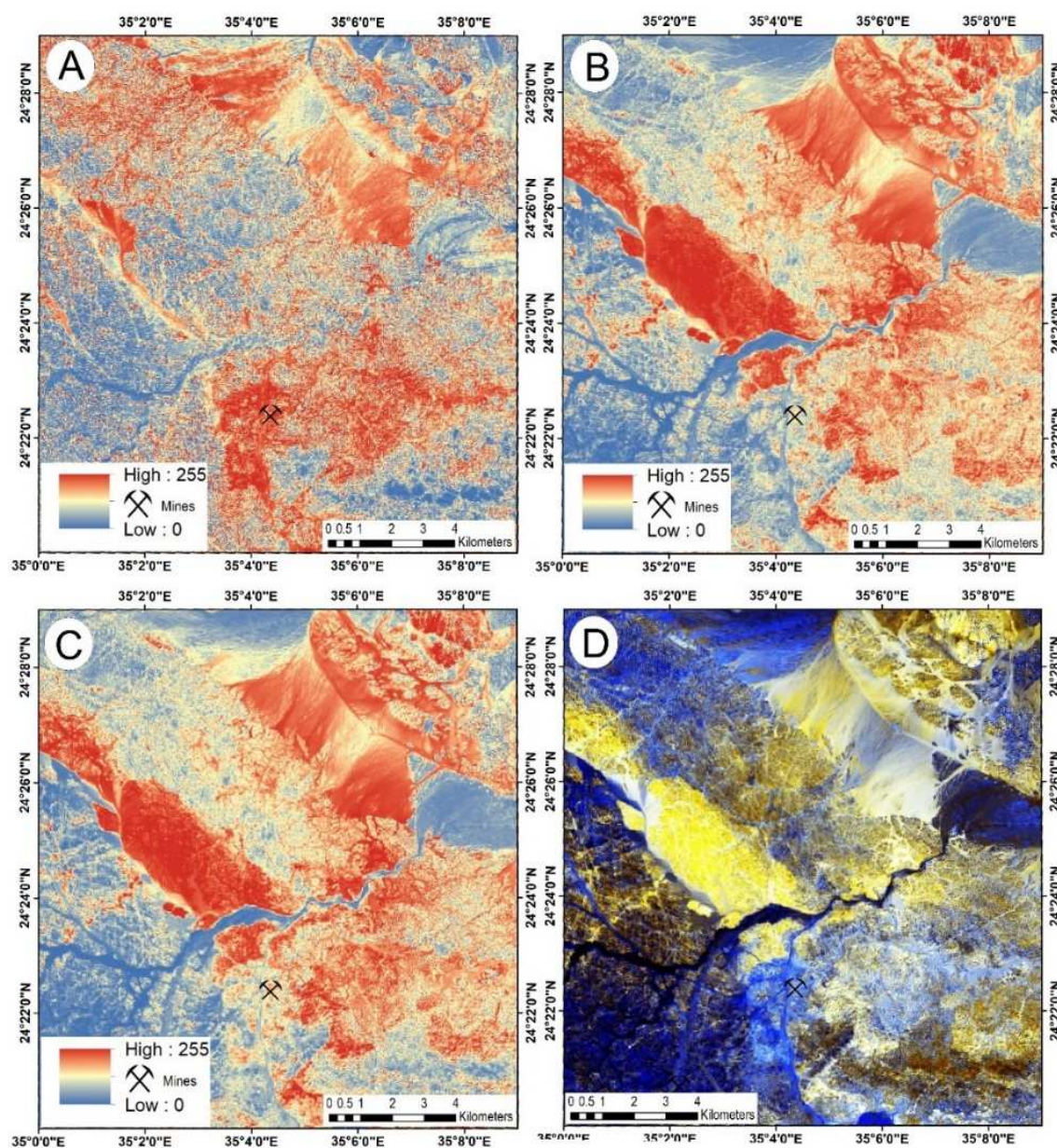


**Figure 9.** Principal component mapping of hydrothermal alterations: (A) Negated PC4 imagery for iron alteration mapping. (B) Negated PC3 image for clay alteration mapping. (C) The sum of negated PC3 and PC4 imagery. (D) PCA false-color composite imagery.

**Table 8.** Eigenvector loading for PC bands 2, 4, 5, and 6.

Eigenvector	Band 2	Band 4	Band 5	Band 6
PC 1	0.273741	0.464852	0.53607	0.649313
PC 2	0.399449	0.421209	0.331573	−0.7437
PC 3	0.730148	0.104788	−0.65623	0.158943
PC 4	0.482069	−0.7717	0.414786	0.006789

Application of PC analysis to bands 2, 5, 6, and 7 suggests information on clay alteration was spatially mapped into PC band 3 as dark pixels. This is evident by negative loading from band 6 accompanied by positive Eigenvector loading from band 7 (Table 9). The generated PC3 data was negated to display the spatial variations in clay alterations as variations from blue (low) to red (high) pixels (Figure 9B).

**Table 9.** Eigenvector loading for PC bands 2, 5, 6, and 7.

Eigenvector	Band 2	Band 5	Band 6	Band 7
PC 1	0.262994	0.515968	0.630105	0.517281
PC 2	0.430685	0.634116	−0.19731	−0.61113
PC 3	0.358168	0.10182	−0.71682	0.589505
PC 4	0.785532	−0.56684	0.224062	−0.10691

A generated false-color composite image based on the integration of the negated PC3 image, the sum of the negated PC3 and PC4 images (Figure 9C), and the negated PC4 image displayed zones of hydrothermal alterations as white, zones of clay alterations as reddish–brown, and zones of intense iron alterations as blue pixels. Yellow represented zones dominated by clay alterations, while cyan represented zones dominated by the presence of iron alterations (Figure 9). Close observation suggests zones of high iron alteration shown in Figure 9A coincide with known occurrences of ilmenite mineralization. Selective principal component analysis using Landsat for alteration mapping was first proposed by [40] but has been highly successful in mapping mineral deposits of diverse origin, and within the Egyptian desert, this approach has been successful in mapping iron deposits [67].

#### 4.5. Alteration Mapping with ASTER Imagery

The spatial and spectral resolution of ASTER sensors facilitates precise mapping of mineral alteration assemblages [68]. ASTER mapping of hydrothermal alteration using band ratio was implemented using band ratios 4/6, 5/6, 5/8, 2/1, and (5/3 + 1/2). Based on spatial reflectance analysis, information on argillic alteration was mapped from blue (low) to red (high) pixels using band ratio 4/6 (Figure 10A), while spatial information on phyllic alteration was displayed from blue (low) to red (high) pixels using band ratio 5/6 (Figure 10B). Band ratio 5/8 imagery displayed variations in propylitic alteration from blue (low) to red (high) (Figure 10C), while band ratio 2/1 displayed from blue (low) to red (high) pixels information related to ferric iron alteration (Figure 6D). Spatial variation in ferrous iron alteration was displayed from blue (low) to red (high) using band ratio (5/3 + 1/2) (Figure 10E). A band-ratio false-color composite of 4/6, 5/6, and 5/8 displayed argillic altered zones as red pixels, phyllic altered zones were green, and propylitic altered zones were blue (Figure 10F). The ASTER band-ratio technique has been very successful and consistent in mapping numerous mineral alterations [33,69].

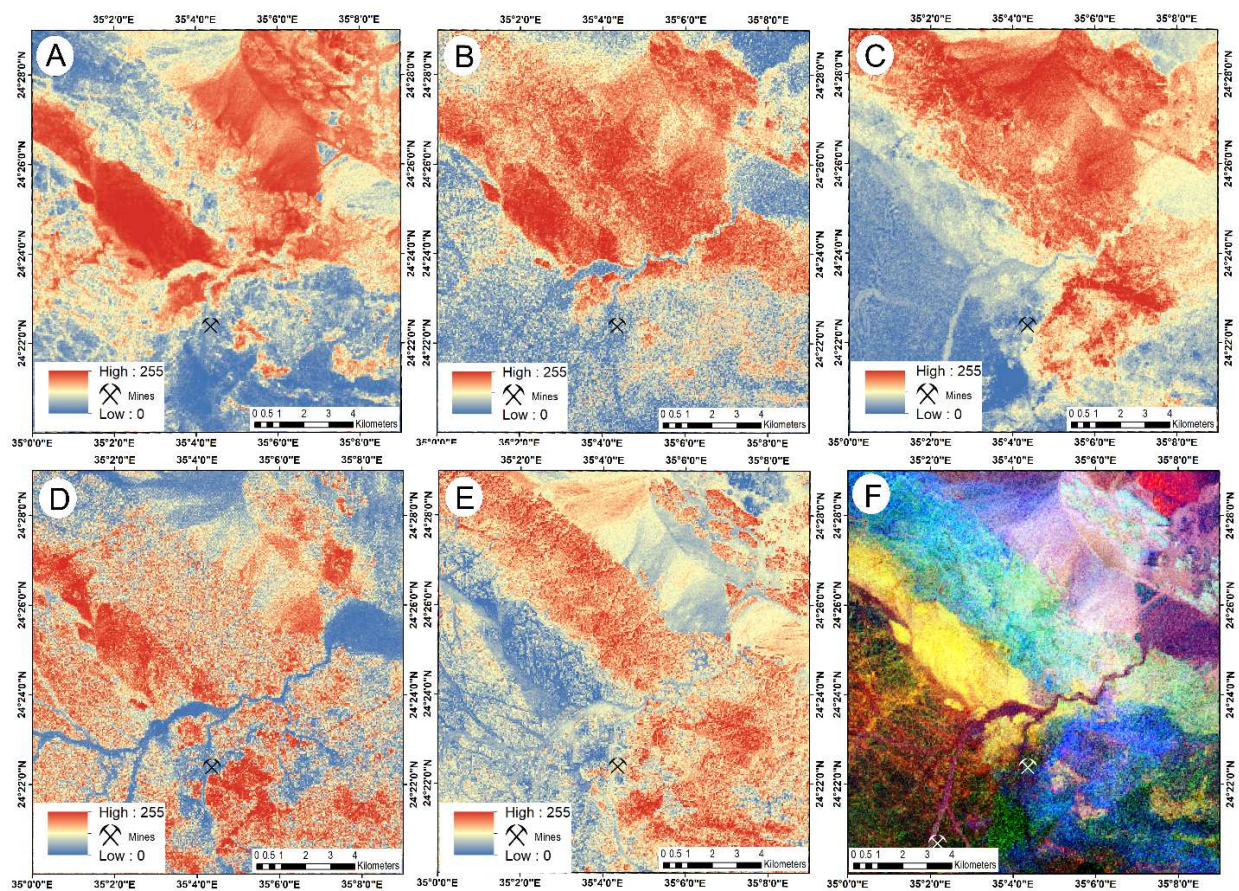


**Figure 10.** ASTER image processing using band ratio: (A) Argillic alteration mapping using band 4/6. (B) Phyllic alteration mapping using band ratio 5/6. (C) Propylitic alteration mapping using band ratio 5/8. (D) Ferric iron alteration mapping using band ratio 2/1. (E) Ferrous iron alteration using band ratio 5/3 + 1/2. (F) Band-ratio false-color composite for ratio imagery 4/6, 5/6, and 5/8.

The application of PCA to ASTER bands 1, 4, 6, and 7 suggests information on argillic alteration was successfully mapped into a principal component as bright pixels into principal component 2 image (Figure 11A). This is evident by a high positive contribution from band 4 accompanied by a low negative contribution from band 6 (Table 10).

The application of PCA to ASTER bands 1, 3, 5, and 6 mapped spatial information on phyllic alteration as dark pixels in the resultant PC3 image. Based on Eigenvector statistics, high negative input was observed for band 5, with an equal positive loading for band 6 (Table 11). The PC3 image was negated to map spatial information on phyllic alteration as bright pixels (Figure 11B). Spatial mapping of propylitic alteration was implemented by application of PCA to ASTER bands 1, 3, 5, and 8 (Figure 11C). Evidence from the resultant Eigenvector statistics suggests information on propylitic alteration was spatially mapped as bright pixels into principal component band 2 images. This is evident by the high positive input from band 5 and a low negative input from band 8 (Table 12).

Figure 11D illustrates a false-color composite PC2 image (argillic alteration), negated PC3 image (phyllic alteration), and PC2 image (propylitic alteration). Yellow pixels within this image represent zones of hydrothermal alterations, while the red pixels are evidence of argillic alterations. The green pixels represent zones associated with phyllic alterations, and the blue pixels are zones of propylitic alterations.

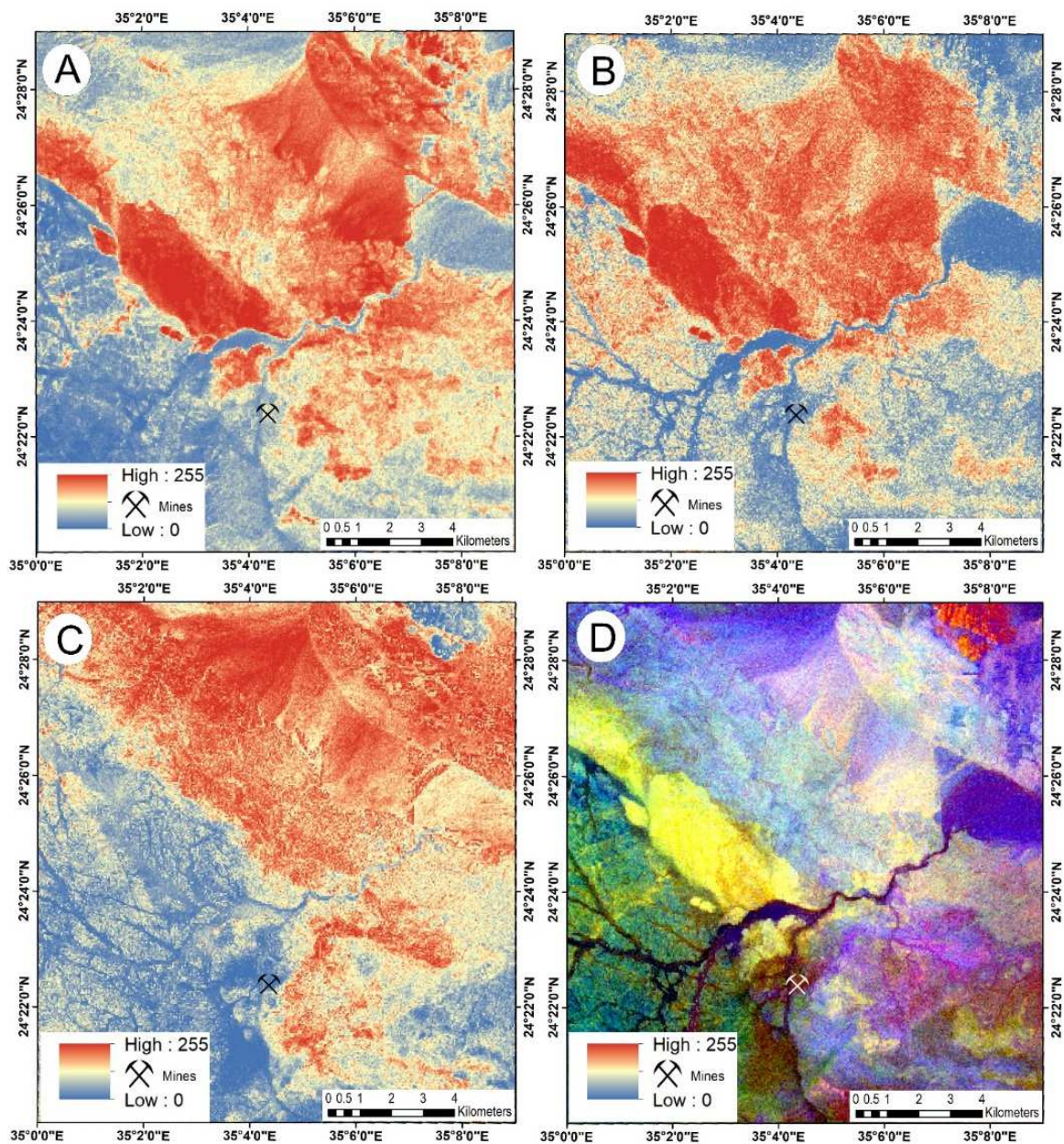


**Figure 11.** (A) PC2 image from PC analysis of bands 1467; (B) negated PC3 image from PC analysis of bands 1, 3, 5, and 6; (C) PC2 image from PC analysis of bands 1, 3, 5, and 8; (D) PC false-color composite image of negated PC4, negated PC3, and PC2 image.

**Table 10.** Eigenvector loading for PC bands 1, 4, 6, and 7.

Eigenvector	Band 1	Band 4	Band 6	Band 7
PC1	0.358965	0.663078	0.445818	0.482408
PC2	−0.19213	0.741133	−0.44609	−0.46348
PC3	0.907729	−0.10509	−0.34811	−0.2093
PC4	−0.10128	0.002287	−0.6936	0.713207

**Table 11.** Eigenvector loading for PC bands 1, 3, 5, and 6.

Eigenvector	Band 1	Band 3	Band 5	Band 6
PC1	0.407388	0.563083	0.51611	0.500603
PC2	0.35935	0.624838	−0.509	−0.47049
PC3	0.50742	−0.33813	−0.5679	0.552887
PC4	0.6689	−0.42212	0.389918	−0.47154

**Table 12.** Eigenvector loading for PC bands 1, 3, 5, and 8.

Eigenvector	Band 1	Band 3	Band 5	Band 8
PC 1	0.425347	0.591601	0.53095	0.432644
PC2	−0.16961	−0.36918	0.840096	−0.35941
PC3	−0.39785	−0.39938	0.095173	0.820458
PC4	−0.795	0.595155	0.057209	−0.10244

4.6. Application of Lineament Analysis

Figure 12 illustrates the general lineament map for the study location. Visual observation of this image suggests lineaments are diverse in orientation but mainly trend in the NW–SE direction. The heterogeneous trends associated with lineaments within the study location are suggestive of a complex tectonic history [70]. The lineaments were concentrated in the center (at the ilmenite mine) to the south, with a high degree of fracturing and density, and the compression progressively expanded northeastward according to the results of the lineament density study (Figure 12A). According to [71], zones of high lineament density are pivotal for the localization of mineral deposits (Figure 12B).

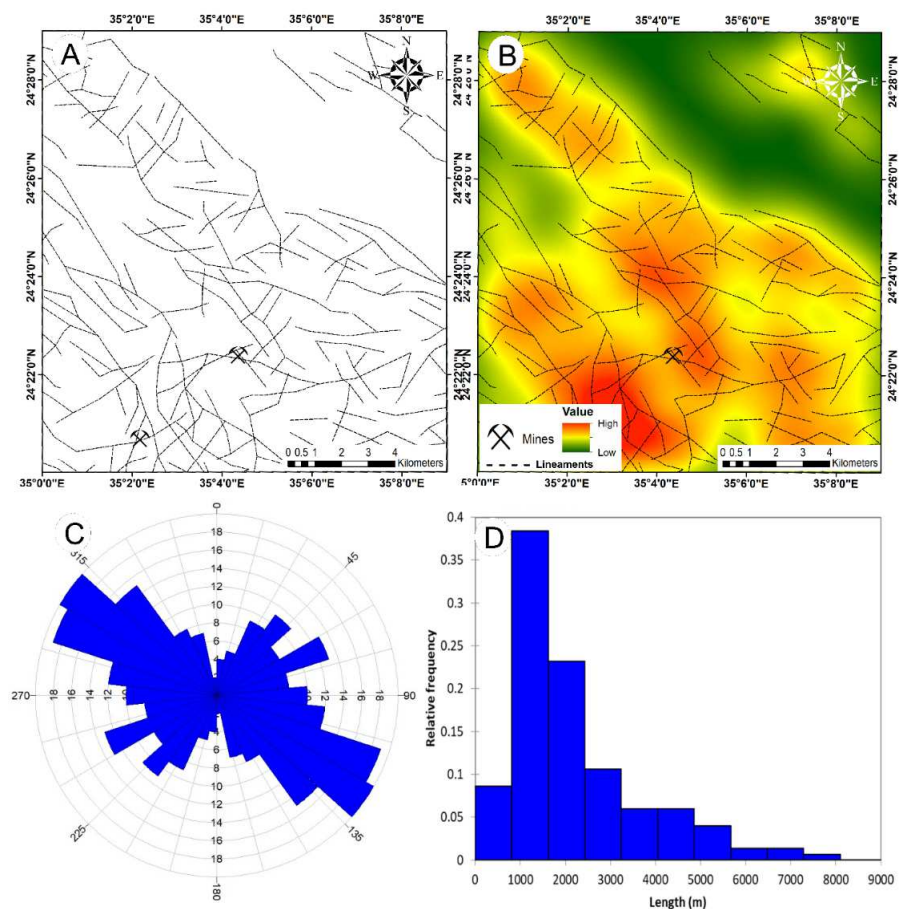


**Figure 12.** (A) Lineament distribution across the study location. (B) Lineament density analysis for the study location. (C) Rose diagram plot for lineaments. (D) Histogram plot for lineament length.

Analysis of rose diagram plots (Figure 12C) for these lineaments suggests the prevalence of the NW–SE direction in association with a less dominant ENE–WSW trend. [72] considered the NW–SE lineaments within the Eastern Egyptian desert as left-lateral strike-slip faults and the ENE–WSW as right and left lateral slip faults. Lineament length for the study location is defined as a maximum of 8066.4 m, a minimum of 63.8 m, a mean of 2132.8 m, and a standard deviation of 1508.9 m. In addition, a histogram length for lineament length suggests negative skew attributes (Figure 12D).

## 5. Conclusions

1. This paper demonstrates that combining remote sensing data with petrographic and geochemical characterization to define hydrothermal alteration zones is a useful technique.
2. The primary goal of the proposed Landsat 8 and ASTER investigations was to categorize the various types of hydrothermal alteration and structural lineaments around the Abu-Ghalaga area.
3. According to Landsat 8 imaging, band ratio 6/7 was used to demonstrate clay change, band ratio 6/5 was used to differentiate zones of ferrous iron alterations, and band ratio 4/2 was used to highlight differences in ferric iron.
4. On the other hand, ASTER mapping of hydrothermal alteration using band-ratio was implemented using band ratios 4/6, 5/6, 5/8, 2/1, and (5/3+1/2). Argillic alteration was recorded on band ratio 4/6, phyllic alteration was displayed on band ratio 5/6, propylitic alteration was visible in band ratio 5/8 imagery, and ferric iron alteration was seen in band ratio 2/1 imagery. Band ratio (5/3+1/2) was used to show spatial variation in ferrous iron alteration.
5. Rose diagram analysis revealed the main structure directions, with ENE–WSW being the most prominent.
6. The study area has been subjected to great tectonic movements, especially those associated with the intervention of the biotite gneissose granites and gabbro. These led to the development of many joints, faults, and fractures in the central part of the region (behind the ilmenite mine).
7. The basement rocks of the Wadi Abu Ghalaga area mainly consist of arc metavolcanic, gabbro–diorite, granodiorite, and tonalite.
8. Field geologic studies demonstrate three forms of alteration: propylitic, phyllic, and argillic.
9. Important alteration minerals according to petrographic investigations are epidotization, sericitization, muscovitization, kaolinitization, and chloritization, which are documented because of high deformation following regional metamorphism in the area.
10. Geochemical results of the rock samples show chlorite–albite–sericite–kaolinite carbonate alteration.

**Author Contributions:** Conceptualization, H.M.E.-D., A.W.T. and A.M.A.-R.; data curation, H.A.A., H.M.H.Z. and A.E.; formal analysis, H.M.E.-D., W.F., H.E.-A. and H.A.A.; funding acquisition, A.E.; investigation, A.M.A.-R., H.A.A., H.M.H.Z., W.F., H.E.-A. and A.E.; methodology, H.M.E.-D. and A.W.T.; project administration, H.A.A., H.M.H.Z. and A.E.; resources, H.M.E.-D., A.W.T. and A.M.A.-R.; software, W.F., A.M.A.-R. and H.E.-A.; supervision, H.M.E.-D., A.W.T., A.M.A.-R. and A.E.; validation, H.E.-A., H.A.A., H.M.H.Z., W.F. and A.E.; visualization, H.A.A. and H.M.H.Z.; writing—original draft, H.M.E.-D., A.W.T. and A.M.A.-R.; writing—review and editing, H.A.A., H.M.H.Z., H.M.E.-D., A.M.A.-R. and A.E. All authors have read and agreed to the published version of the manuscript.

**Funding:** The APC is funded by “Dunarea de Jos”, University of Galati, Romania.

**Data Availability Statement:** Not applicable.

**Acknowledgments:** The APC is funded by “Dunarea de Jos” University of Galati, Romania. H.A.A. is funded by a scholarship under the Joint Executive Program between Egypt and Russia.

**Conflicts of Interest:** The authors declare no conflict of interest.

## References

1. Honarmand, M.; Ranjbar, H.; Shahabpour, J. Application of principal component analysis and spectral angle mapper in the mapping of hydrothermal alteration in the Jebal-Barez Area, Southeastern Iran. *Resour. Geol.* **2012**, *62*, 119–139. [[CrossRef](#)]
2. Shahriari, H.; Ranjbar, H.; Honarmand, M. Image segmentation for hydrothermal alteration mapping using PCA and concentration–area fractal model. *Nat. Resour. Res.* **2013**, *22*, 191–206. [[CrossRef](#)]
3. Mahboob, M.A.; Atif, I.; Iqbal, J. Remote sensing and GIS applications for assessment of urban sprawl in Karachi, Pakistan. *Sci. Technol. Dev.* **2015**, *34*, 179–188. [[CrossRef](#)]
4. Harris, J.R.; Rencz, A.N.; Ballantyne, B.; Sheridon, C. Mapping altered rocks using LANDSAT TM and lithochemical data: Sulphurets-Brucejack Lake district, British Columbia, Canada. *Photogramm. Eng. Remote Sens.* **1998**, *64*, 309–322.
5. Frutuoso, R.; Lima, A.; Teodoro, A.C. Application of remote sensing data in gold exploration: Targeting hydrothermal alteration using Landsat 8 imagery in northern Portugal. *Arab. J. Geosci.* **2021**, *14*, 1–18. [[CrossRef](#)]
6. Tende, A.W.; Mustapha, T.; Fru, M.I.N.; Gajere, J.N.; Aminu, M.D. Hybrid extraction of tectonic lineaments from digital elevation model. *Appl. Geomat.* **2022**, *14*, 163–180. [[CrossRef](#)]
7. Basta, E.Z.; Takla, M.A. Mineralogy and origin of Abu Ghalaga ilmenite occurrence, Eastern Desert. *J. Geol.* **1968**, *12*, 87–124.
8. El Ramly, M.F. A new geological map for the basement rocks in the Eastern and Southwestern desert of Egypt: Scale 1: 1,000,000. *Ann. Geol. Surv. Egypt* **1972**, *2*, 1–8.
9. Salem, S.M.; El Gammal, E.A. Iron ore prospection East Aswan, Egypt, using remote sensing techniques. *Egypt. J. Remote Sens. Sp. Sci.* **2015**, *18*, 195–206. [[CrossRef](#)]
10. Abdou, M.I.; Moustafa, M.A.E.-F.; Ahmed, H.E.-S.; El-Wahab, H.A. Utilization of Egyptian ilmenite ore for steel surface preparation in petroleum field. *Engineering* **2011**, *3*, 802. [[CrossRef](#)]
11. Maurice, A.E.; Basta, F.F.; Khiamy, A.A. Neoproterozoic nascent island arc volcanism from the Nubian Shield of Egypt: Magma genesis and generation of continental crust in intra-oceanic arcs. *Lithos* **2012**, *132*, 1–20. [[CrossRef](#)]
12. Ramadan, A.M.; Farghaly, M.; Fathy, W.M.; Ahmed, M.M. Leaching and kinetics studies on processing of Abu-Ghalaga ilmenite ore. *Int. Res. J. Eng. Tech.* **2016**, *3*, 46–53.
13. Salem, S.M. ASD field hyperspectral measurements for discrimination of the ferruginous rocks and the iron ore types at El Gedida-Ghorabi area, Bahariya Oasis, Western Desert, Egypt. *Arab. J. Geosci.* **2017**, *10*, 1–13. [[CrossRef](#)]
14. Awad, H.A.; Nastavkin, A.V. Geochemical and Geotectonic Setting for Island Arc Related rocks on Um Taghir Area, Central Eastern Desert, Egypt. In Proceedings of the IOP Conference Series: Earth and Environmental Science, Vladivostok, Russia, 25–26 January 2021; IOP Publishing: Bristol, UK, 2021; Volume 720, p. 12049.
15. Ali, K.A.; Andresen, A.; Stern, R.J.; Manton, W.I.; Omar, S.A.; Maurice, A.E. U-Pb zircon and Sr-Nd-Hf isotopic evidence for a juvenile origin of the c 634 Ma El-Shalul granite, Central Eastern Desert, Egypt. *Geol. Mag.* **2012**, *149*, 783–797. [[CrossRef](#)]
16. Hassan, M.A.; Hashad, A.H. Precambrian of Egypt. In *The Geology of Egypt*; Routledge: London, UK, 1990; Volume 201, p. 248.
17. Mohamed, F.H.; Moghazi, A.M.; Hassanen, M.A. Geochemistry, petrogenesis and tectonic setting of late Neoproterozoic Dokhan-type volcanic rocks in the Fatira area, eastern Egypt. *Int. J. Earth Sci.* **2000**, *88*, 764–777. [[CrossRef](#)]
18. Ali, K.A.; Azer, M.K.; Gahlan, H.A.; Wilde, S.A.; Samuel, M.D.; Stern, R.J. Age constraints on the formation and emplacement of Neoproterozoic ophiolites along the Allaqi-Heiani Suture, South Eastern Desert of Egypt. *Gondwana Res.* **2010**, *18*, 583–595. [[CrossRef](#)]
19. Stern, R.J.; Hedge, C.E. Geochronologic and isotopic constraints on late Precambrian crustal evolution in the Eastern Desert of Egypt. *Am. J. Sci.* **1985**, *285*, 91–127. [[CrossRef](#)]
20. Willis, K.M.; Stern, R.J.; Clauer, N. Age and geochemistry of Late Precambrian sediments of the Hammamat Series from the Northeastern Desert of Egypt. *Precambrian Res.* **1988**, *42*, 173–187. [[CrossRef](#)]
21. Moussa, E.M.M.; Stern, R.J.; Manton, W.I.; Ali, K.A. SHRIMP zircon dating and Sm/Nd isotopic investigations of Neoproterozoic granitoids, Eastern Desert, Egypt. *Precambrian Res.* **2008**, *160*, 341–356. [[CrossRef](#)]
22. Wilde, S.A.; Youssef, K. Significance of SHRIMP U-Pb dating of the imperial porphyry and associated Dokhan volcanics, Gebel Dokhan, north Eastern Desert, Egypt. *J. Afr. Earth Sci.* **2000**, *31*, 403–413. [[CrossRef](#)]
23. Hashad, A.H.; Al Shanti, A.M.S. Present status of geochronological data on the Egyptian basement complex. *Evol. Miner. Arab. Shield* **1980**, *1*, 31–46.
24. Stern, R.J. Petrogenesis and tectonic setting of Late Precambrian ensimatic volcanic rocks, Central Eastern Desert of Egypt. *Precambrian Res.* **1981**, *16*, 195–230. [[CrossRef](#)]
25. Ali, B.H.; Wilde, S.A.; Gabr, M.M.A. Granitoid evolution in Sinai, Egypt, based on precise SHRIMP U-Pb zircon geochronology. *Gondwana Res.* **2009**, *15*, 38–48. [[CrossRef](#)]
26. Kröner, A.; Todt, W.; Hussein, I.M.; Mansour, M.; Rashwan, A. Dating of late Proterozoic ophiolites in Egypt and the Sudan using the single grain zircon evaporation technique. *Precambrian Res.* **1992**, *59*, 15–32. [[CrossRef](#)]
27. Abdel-Monem, A.A.; Hurlley, P.M. U-Pb dating of zircons from psammitic gneisses, Wadi Abu Rosheid-Wadi Sikait area, Egypt. In *Evolution and Mineralization of the Arabian-Nubian Shield: Proceedings of a Symposium*; Pergamon Press: Oxford, UK, 1979; Volume 1, p. 165.
28. Abrams, M.; Crippen, R.; Fujisada, H. ASTER global digital elevation model (GDEM) and ASTER global water body dataset (ASTWBD). *Remote Sens.* **2020**, *12*, 1156. [[CrossRef](#)]

29. dos Santos, M.A.; van Lier, Q.D.; van Dam, J.C.; Freire, A.H. Determination of empirical parameters for root water uptake models. *Hydrol. Earth Syst. Sci. Discuss.* **2016**, *21*, 473–493. [CrossRef]
30. Richter, R.; Schläpfer, D.; Müller, A. Operational atmospheric correction for imaging spectrometers accounting for the smile effect. *IEEE Trans. Geosci. Remote Sens.* **2010**, *49*, 1772–1780. [CrossRef]
31. Wambo, J.D.T.; Pour, A.B.; Ganno, S.; Asimow, P.D.; Zoheir, B.; dos Reis Salles, R.; Nzenti, J.P.; Pradhan, B.; Muslim, A.M. Identifying high potential zones of gold mineralization in a sub-tropical region using Landsat-8 and ASTER remote sensing data: A case study of the Ngoura-Colomines goldfield, eastern Cameroon. *Ore Geol. Rev.* **2020**, *122*, 103530. [CrossRef]
32. Traore, M.; Wambo, J.D.T.; Ndepete, C.P.; Tekin, S.; Pour, A.B.; Muslim, A.M. Lithological and alteration mineral mapping for alluvial gold exploration in the south east of Birao area, Central African Republic using Landsat-8 Operational Land Imager (OLI) data. *J. Afr. Earth Sci.* **2020**, *170*, 103933. [CrossRef]
33. Andongma, W.T.; Gajere, J.N.; Amuda, A.K.; Edmond, R.R.D.; Faisal, M.; Yusuf, Y.D. Mapping of hydrothermal alterations related to gold mineralization within parts of the Malumfashi Schist Belt, North-Western Nigeria. *Egypt. J. Remote Sens. Sp. Sci.* **2021**, *24*, 401–417. [CrossRef]
34. San, B.T.; Sumer, E.O.; Gurcay, B. Comparison of band ratioing and spectral indices methods for detecting alunite and kaolinite minerals using ASTER data in Biga region, Turkey. In *Proceedings ISPRS*; ISPRS: Hannover, Germany, 2004.
35. Inzana, J.; Kusky, T.; Higgs, G.; Tucker, R. Supervised classifications of Landsat TM band ratio images and Landsat TM band ratio image with radar for geological interpretations of central Madagascar. *J. Afr. Earth Sci.* **2003**, *37*, 59–72. [CrossRef]
36. Nair, A.; Mathew, G. Lithological discrimination of the phenaimata felsic–mafic complex, Gujarat, India, using the advanced spaceborne thermal emission and reflection radiometer (ASTER). *Int. J. Remote Sens.* **2012**, *33*, 198–219. [CrossRef]
37. da Cunha Frutuoso, R.M. Mapping Hydrothermal Gold Mineralization Using Landsat 8 Data. A Case of Study in Chaves License, Portugal. 2015. Available online: <https://repositorio-aberto.up.pt/bitstream/10216/86528/2/127594.pdf> (accessed on 6 June 2022).
38. Sheikhrhimi, A.; Pour, A.B.; Pradhan, B.; Zoheir, B. Mapping hydrothermal alteration zones and lineaments associated with orogenic gold mineralization using ASTER data: A case study from the Sanandaj-Sirjan Zone, Iran. *Adv. Sp. Res.* **2019**, *63*, 3315–3332. [CrossRef]
39. Ghulam, A.; Amer, R.; Kusky, T.M. Mineral exploration and alteration zone mapping in Eastern Desert of Egypt using ASTER Data. In *Proceedings of the ASPRS 2010 Annual Conference*, San Diego, CA, USA, 26–30 April 2010.
40. Crosta, A.P.; MOORE, J.M. Geological mapping using Landsat thematic mapper imagery in Almeria Province, South-East Spain. *Int. J. Remote Sens.* **1989**, *10*, 505–514. [CrossRef]
41. Bell, F.G. The physical and mechanical properties of the fell sandstones, Northumberland, England. *Eng. Geol.* **1978**, *12*, 1–29. [CrossRef]
42. Tripp, G.I.; Vearncombe, J.R. Fault/fracture density and mineralization: A contouring method for targeting in gold exploration. *J. Struct. Geol.* **2004**, *26*, 1087–1108. [CrossRef]
43. Sadiq, S.; Muhammad, U.; Fuchs, M. Investigation of landslides with natural lineaments derived from integrated manual and automatic techniques applied on geospatial data. *Nat. Hazards* **2022**, *110*, 2141–2162. [CrossRef]
44. Abdul Malik, N.F.; Garba, I.; Danbatta, U.A.; Hamza, H. Delineation and correlation of lineaments using landsat-7 ETM+, DEM and aeromagnetic datasets: Basement complex of shanono, northwestern Nigeria. *J. Geol. Geophys* **2018**, *7*, 445.
45. Weerasekara, W.L.; Mayadunna, B.B.; Senanayake, I.P.; Dissanayake, D. Integrated remote sensing and GIS in lineament mapping for groundwater exploration—A case study in Ambalantota, Sri Lanka. In *Proceeding of SAIMT Research Symposium on Engineering Advancements*; South Asian Institute of Technology and Medicine: Malabe, Sri Lanka, 2014; p. 62e65.
46. Immaculate, N.-F.M.; Tende, A.W.; Fouateu, Y.R.; Marc, A.F.Q. Remote sensing for geological investigation of Mayo Kila and environs, north west region of Cameroon. *Am. J. Earth Sci.* **2020**, *7*, 1–12.
47. Hung, L.Q.; Batelaan, O.; De Smedt, F. Lineament extraction and analysis, comparison of LANDSAT ETM and ASTER imagery. Case study: Suoimuoi tropical karst catchment, Vietnam. In *Proceedings of the Remote Sensing for Environmental Monitoring, GIS Applications, and Geology V*, Bruges, Belgium, 19–22 September 2005; Volume 5983, pp. 182–193.
48. Ridley, J. *Ore Deposit Geology*; Cambridge University Press: Cambridge, UK, 2013; ISBN 1107022223.
49. Hall, A. The influence of secondary alteration on the ammonium content of granites, exemplified by the Rosses complex of Donegal. *Mineral. Mag.* **1993**, *57*, 591–598. [CrossRef]
50. Browne, P.R.L. Hydrothermal alteration in active geothermal fields. *Annu. Rev. Earth Planet. Sci.* **1978**, *6*, 229–250. [CrossRef]
51. Streckeisen, A. Classification of the Common Igneous Rocks by Means of Their Chemical Composition: A Provisional Attempt. *Neues Jahrb. Mineral.* **1976**, *1*, 1.
52. Irvine, T.N.J.; Baragar, W.R.A. A guide to the chemical classification of the common volcanic rocks. *Can. J. Earth Sci.* **1971**, *8*, 523–548. [CrossRef]
53. Maniar, P.D.; Piccoli, P.M. Tectonic discrimination of granitoids. *Geol. Soc. Am. Bull.* **1989**, *101*, 635–643. [CrossRef]
54. Jensen, L.S. A new plot for classifying subalkalic volcanic rocks. *Ont. Div. Mines Misc. Pap.* **1976**, *66*, 1–22.
55. Green, T.; Roberts, D. The Holonda porphyrite, Norwegian Caledonides: Geochemistry and tectonic setting of Early–Mid-Ordovician shoshonitic volcanism. *J. Geol. Soc.* **1998**, *155*, 131–142. [CrossRef]
56. Pearce, J.A.; Harris, N.B.W.; Tindle, A.G. Trace element discrimination diagrams for the tectonic interpretation of granitic rocks. *J. Petrol.* **1984**, *25*, 956–983. [CrossRef]

57. Middlemost, E.A.K. Naming materials in the magma/igneous rock system. *Earth-Sci. Rev.* **1994**, *37*, 215–224. [[CrossRef](#)]
58. Shand, S.J. On the relations between silica, alumina, and the bases in eruptive rocks, considered as a means of classification. *Geol. Mag.* **1927**, *64*, 446–449. [[CrossRef](#)]
59. Cuney, M.; Friedrich, M. Physicochemical and crystal-chemical controls on accessory mineral paragenesis in granitoids: Implications for uranium metallogenesis. *Bull. Mineral.* **1987**, *110*, 235–247. [[CrossRef](#)]
60. Large, R.R.; Gemell, J.B.; Paulick, H.; Huston, D.L. The alteration box plot: A simple approach to understanding the relationship between alteration mineralogy and litho geochemistry associated with volcanic-hosted massive sulfide deposits. *Econ. Geol.* **2001**, *96*, 957–971. [[CrossRef](#)]
61. Ishikawa, Y.; Sawaguchi, T.; Iwaya, S.; Horiuchi, M. Delineation of prospecting targets for Kuroko deposits based on modes of volcanism of underlying dacite and alteration haloes. *Min. Geol.* **1976**, *26*, 105–117.
62. Meyer, C. Wall Rock Alteration. In *Geochemistry of Hydrothermal Ore Deposits*; John Wiley & Sons: Hoboken, NJ, USA, 1967; pp. 166–235.
63. Wu, M.; Zhou, K.; Wang, Q.; Wang, J. Mapping hydrothermal zoning pattern of porphyry Cu deposit using absorption feature parameters calculated from ASTER data. *Remote Sens.* **2019**, *11*, 1729. [[CrossRef](#)]
64. Moradi, R.; Boomeri, M. Remote sensing detection of altered zones associated with Cu-Mo mineralization in North of Zahedan, SE Iran using Landsat-8 data. *Yerbilimleri* **2017**, *38*, 275–294.
65. Mia, B.; Fujimitsu, Y. Mapping hydrothermal altered mineral deposits using Landsat 7 ETM+ image in and around Kuju volcano, Kyushu, Japan. *J. Earth Syst. Sci.* **2012**, *121*, 1049–1057. [[CrossRef](#)]
66. Zoheir, B.; Emam, A. Integrating geologic and satellite imagery data for high-resolution mapping and gold exploration targets in the South Eastern Desert, Egypt. *J. Afr. Earth Sci.* **2012**, *66*, 22–34. [[CrossRef](#)]
67. Kamel, M.; Youssef, M.; Hassan, M.; Bagash, F. Utilization of ETM+ Landsat data in geologic mapping of wadi Ghadir-Gabal Zabara area, Central Eastern Desert, Egypt. *Egypt. J. Remote Sens. Sp. Sci.* **2016**, *19*, 343–360. [[CrossRef](#)]
68. Shirmard, H.; Farahbakhsh, E.; Beiranvand Pour, A.; Muslim, A.M.; Müller, R.D.; Chandra, R. Integration of selective dimensionality reduction techniques for mineral exploration using ASTER satellite data. *Remote Sens.* **2020**, *12*, 1261. [[CrossRef](#)]
69. Fatima, K.; Khattak, M.U.K.; Kausar, A.B.; Toqeer, M.; Haider, N.; Rehman, A.U. Minerals identification and mapping using ASTER satellite image. *J. Appl. Remote Sens.* **2017**, *11*, 46006. [[CrossRef](#)]
70. Yusuf, S.N.; Kuku, A.Y.; Ibrahim, Y.; Kasidi, S. Tectono-metamorphic deformation and structures of Mubi-Hong area, NE, Nigeria. *Niger. J. Technol. Dev.* **2019**, *16*, 201–212. [[CrossRef](#)]
71. Ananaba, S.E.; Ajakaiye, D.E. Evidence of tectonic control of mineralization in Nigeria from lineament density analysis A Landsat-study. *Int. J. Remote Sens.* **1987**, *8*, 1445–1453. [[CrossRef](#)]
72. Ibrahim, I.H. Impact of Structural Lineaments on Mineralized Occurrences in North Abu Rusheid-Sikait Area, South Eastern Desert, Egypt. In *Proceedings of the 5th Tunisian Days of Applied Geology JTGA 2013, Hammamet, Tunisia, 17–20 May 2013*; pp. 227–251.